nature communications

Article

https://doi.org/10.1038/s41467-025-61275-2

Nanotwinned CrN ceramics with enhanced plasticity

Received: 24 October 2024

Accepted: 15 June 2025

Published online: 01 July 2025

Check for updates

Liangliang Liu[1,4], Xiaokai An[1,4], Xinlei Gu[2,4], Tijun Li[1,4], Dongjie Yang[1], Bingjing Huang[1], Qiang Xu[1], Ziqi Ma[1], Shusheng Chen[1], Kan Zhang[2] ✉, Suihan Cui[1,3] ✉, Paul K. Chu[3] & Zhongzhen Wu[1] ✉

Ceramic materials are usually hard but brittle, and it is challenging to achieve a simultaneous enhancement of strength and plasticity using conventional strengthening methods. In ceramic materials with similar atomic size and properties, the fabrication of nanotwins is a promising approach to enhance the plasticity, but it is unknown whether the strategy works for transition metal nitrides. Herein, nanotwinned CrN (NT-CrN) with a twin density of 9.0×10^{15} m^{-2} and twin-containing grain volume fraction of about 52 % is prepared by adjusting the ion kinetic energy during growth. Owing to the twin boundaries, NT-CrN exhibits high hardness (>36 GPa) and enhanced room-temperature plasticity at the same time. Compression deformation of over 40% without brittle failure is achieved. The enhanced room-temperature plasticity is attributed to the distributions of nanotwin boundaries (nano-TB) which allow special slipping by twisting the polyhedron constructed by nano-TB without bond breakage. The accompanying twin proliferation and fusion subsequently dissipate the energy to enhance the plasticity.

Ceramic materials characterized by high strength, high hardness, and high-temperature resistance are essential for a wide range of industrial and scientific applications[1]. However, compared to metals, ceramics often exhibit greater brittleness, which induces catastrophic fracture under even slight deformation[2]. Therefore, enhancing the deformability and suppressing the initiation and propagation of cracks are paramount challenges to ceramic materials[3–5]. Studies on the improvement of ceramics toughness have mainly focused on second-phase toughening (particles[6], whiskers[7], composite phases[3], etc.) and nanostructure toughening (nanolayers[4], nanocrystalline/amorphous composites[5]). Recently, some in-situ prepared microstructural defects such as dislocations[8,9] and nanotwins[10,11] have been shown to improve the toughness of ceramics, for example, high-density nanotwinned cubic boron nitride and diamond with toughness exceeding 12 MPa $m^{1/2}$ and 9.7–14.8 MPa $m^{1/2}$, respectively, which are comparable to those of cemented carbide[10,11]. Furthermore, deformation behaviors in ceramics have also been reported by designing some special structures. For example, a tensile deformation of over 40% has been achieved in Mo/La_2O_3 using the borrowing-dislocations strategy[12]; 14% compressive strain can be achieved by introducing a twisted laminated structure in boron nitride[13]; and 20% compressive plastic deformation is observed from double-phase Si_3N_4 due to a mechanism involving covalent bond breaking-rotation-rebonding at the coherent interfaces. Therefore, ceramic materials can resist the applied loads through plastic deformation at room temperature similar to metals[2]. Simulations also indicate that introducing nanoscale defects into ceramics can reduce the energy threshold of dislocation slipping, thereby suggesting the potential to achieve room-temperature plasticity[14]. In fact, nanotwins have been demonstrated to facilitate dislocation slipping in the deformation processes of metals, alloys, and covalent-bond ceramics with similar atomic size and properties[10,11,15–17]. However, with regard to transition metal oxide/carbide/nitride ceramic materials (TMO/TMC/TMN), which have larger differences in the atomic size and properties but are used more broadly in the industry, the effects of high-density

[1]School of Advanced Materials, Peking University Shenzhen Graduate School, Shenzhen 518055, China. [2]School of Materials Science and Engineering, Jilin University, Changchun 130012, China. [3]Department of Physics, City University of Hong Kong, Tat Chee Avenue, Kowloon, Hong Kong 999077, China. [4]These authors contributed equally: Liangliang Liu, Xiaokai An, Xinlei Gu, Tijun Li. ✉e-mail: kanzhang@jlu.edu.cn; cuish@pku.edu.cn; wuzz@pku.edu.cn

nanotwins are unknown. Moreover, all previously reported ceramics exhibiting plasticity are wide-bandgap semiconductors or insulators, with no instances reported in conductive ceramics.

In this work, combining high power impulse magnetron sputtering (HiPIMS) and electromagnetic screening technology, an ion source with nearly 100% ionization and controllable ion energy has been developed (see supplementary Fig. 1)[18]. By producing discharges from a Cr target in a mixed atmosphere of nitrogen and argon, a chromium ion beam with an energy of about 100 eV is used to deposit CrN coatings. The highly energetic ions produce strain to promote nucleation of nanotwins and NT-CrN with a high nanotwin density of $9.0 \times 10^{15}\,m^{-2}$ and twin-containing grain volume fraction of about 52 % has been fabricated. The abundance of nanotwins and other polymorphic nanostructures produce structural responses during deformation resulting in a yield strength of 32 GPa. The proliferation and movement of nanotwin boundaries occurring between the Cr and N lattice positions activate dislocation slipping and allow for compressive deformation exceeding 40% without brittle fracture in room-temperature.

Results

The CrN coating has the typical face-centered cubic (FCC) structure with a preferred (200) orientation (Supplementary Fig. 2). Calculations based on the Scherrer equation reveal a grain size of approximately 30.7 nm, which aligns with the statistical data (32 nm) obtained from the TEM images (Supplementary Fig. 3). The EDS results show the ratio of Cr to N is nearly 1:1(Supplementary Fig. 4). The electrical resistivity is about $3.3 \times 10^{-4}\,\Omega\,cm$ which is closed to the metals as displayed in Supplementary Table 1. Figure 1 shows the typical microstructure of the NT-CrN. Three-dimensional reconstruction based on the surface

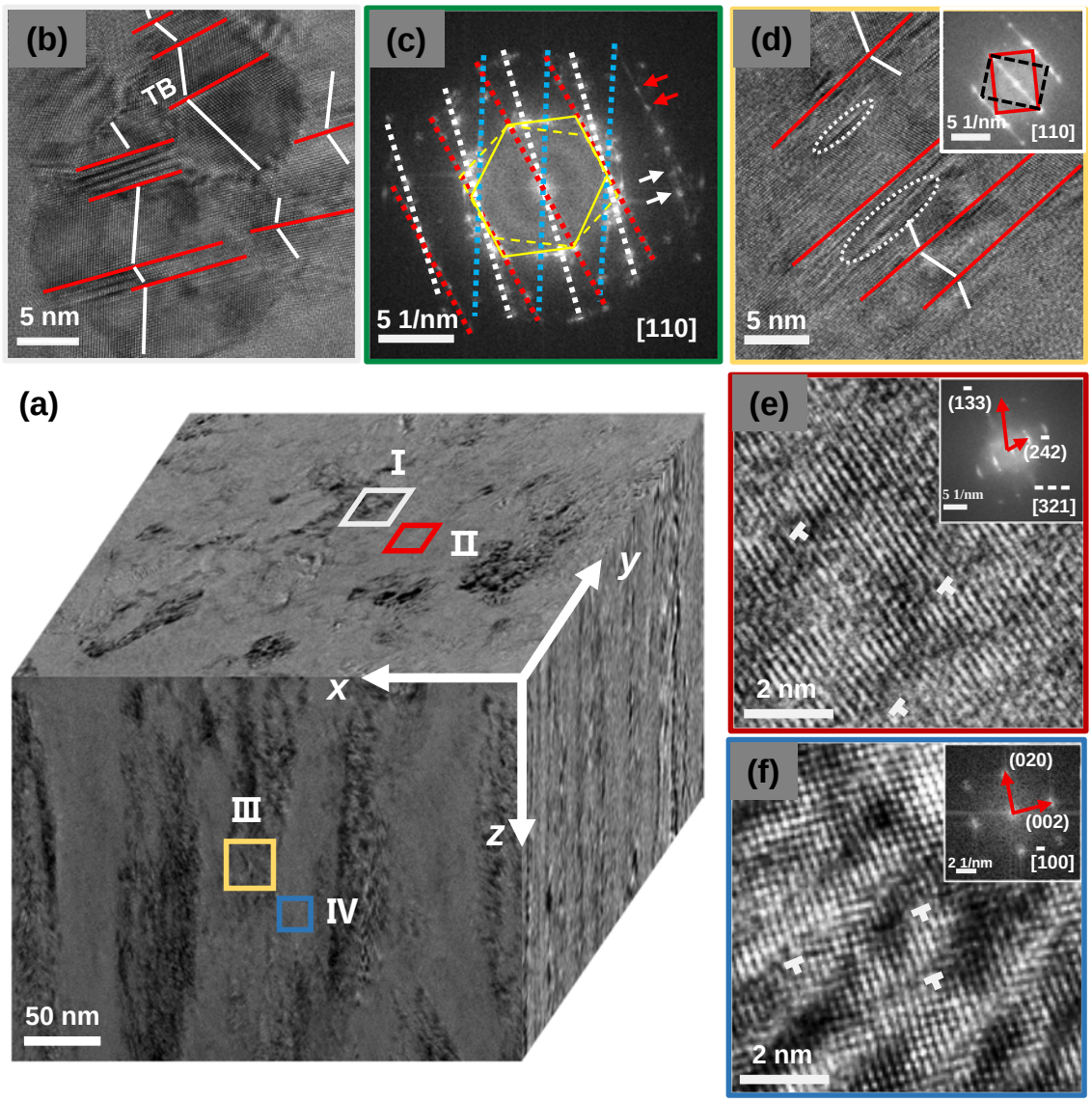

Fig. 1 | Typical microstructures of CrN by bright-field transmission electron microscopy (TEM). a Three-dimensional TEM reconstruction with the grain features within the plane (x-y plane) showing distinct brightness contrast and the cross-section showing the columnar characteristic. **b** High-resolution TEM (HR-TEM) image of the dark-contrast region (I) within the plane with the corresponding Fast Fourier Transform (FFT) in (**c**). The red and white solid lines indicate the twin boundary (TB) and crystal plane, respectively. In the FFT, the red, white, and blue dashed lines indicate different directions of diffraction spots, and the yellow hexagon along with white and red arrows indicates the presence of different moiré fringes. **d** HR-TEM image of the dark-contrast region (III) in the cross-section with the corresponding FFT shown in the inset. The red and black rectangles in the FFT indicate the presence of diffraction moiré fringes. The zones in the white circles display stacking faults. **e** HR-TEM image of the bright-contrast region (II) within the plane with the corresponding FFT in the inset. **f** HR-TEM image of the bright-contrast region (IV) in the cross-section with the corresponding FFT shown in the inset. There are numerous nanoscale twins in the dark-contrast regions (with TBs, marked by red solid lines and crystal planes by white solid lines), while high-density dislocations are present in the bright-contrast regions (indicated by white letter T).

(*x*-*y* plane) and cross-section (*x*(*y*)-*z* plane) TEM images reveals a smooth and dense surface and cross-section. The grains in the coating are closely packed with no noticeable pores, and mutual compression between grains gives rise to irregular grain boundaries (Fig. 1a). There are regions with distinct bright and dark contrasts. High-resolution TEM (HR-TEM) shows darker areas on the surface (Region I) with a multitude of atomic structures with mirror-symmetrical distributions of grains indicative of twin boundaries (TBs)[19]. The TBs appear straight with sizes ranging from a few to several tens of nanometers (Fig. 1b). The electron diffraction lattice obtained by Fast Fourier Transform (FFT) shows (Fig. 1c) multiple diffraction spots from different directions as well as symmetrical spot-sets in the same direction. It can be inferred that the diffraction spots in the symmetric axis correspond to mirror symmetry planes, namely TB. According to Bragg's equation, the TB in this region can be determined to be the (111) plane with the crystallographic axis of <110>. Similarly, in the dark-contrast area in the cross-section (Region III), there are high-density nanotwin structures (Fig. 1d) and between twins, some irregular atomic arrangements with partially continuous and blurred features in the corresponding FFT appear in a smaller size scale, indicating the presence of even smaller lattice defects such as dislocations and stacking faults (SFs) (Fig. 1d inset)[20,21]. Both the bright-contrast areas in the surface and cross-section (Regions II and IV) do not exhibit apparent twin characteristics, but dislocation structures are observed (Fig. 1e, f). The images obtained by inverse fast Fourier transform (Supplementary Fig. 5) also confirm the existence of dislocations. According to the diffraction characteristics, twins in FCC are observed only along {111}<110>, while undetectable along other directions[22]. With the exception of {111}, the FFT diffraction spots corresponding to the bright-contrast region reveal the presence of multiple high-index crystal planes (such as $\{2\bar{4}2\}$ and {020} planes) with the crystallographic axes being $<\bar{3}2\bar{1}>$ and $<\bar{1}00>$, respectively. Therefore, the existence of twinning is probable in this region, but cannot be observed along this specific direction. This phenomenon can also be illustrated through 3D reconstruction image. In the context of 3D reconstruction image, the intersection of two planes corresponds to the same grain, but the contrast varies between the planes. On the black-contrast plane, the twin structure is clearly visible, whereas on the bright-contrast plane, it often appears as dislocations. This observation confirms that twin structures are only observable along specific orientations.

A statistical analysis (Supplementary Fig. 6) is conducted on the widths and quantities of 634 twins (excluding SF) randomly selected from 69 grains observed by high-angle annular dark field scanning transmission electron microscopy (HAADF-STEM). The twin thickness varies from one to several nanometers, with approximately 43% of twins in the range of 2–4 nm. The average twin size is about 3.8 nm, and each grain on average contains 9.2 twins (Supplementary Fig. 6b). The twin density is approximately $9.0 \times 10^{15} m^{-2}$, calculated from both the dark and bright regions. Additionally, the volume fraction of twin-containing grains is also calculated by randomly selecting 200 grains, which is about 52%, comparable to that of nano-twinned Cu[23,24]. Generally, achieving a high density of nanotwins in ceramics is particularly challenging due to their high stacking fault energy[25,26]. Energy regulation is crucial for overcoming the energy barrier and inducing twin formation[27]; however, excessive energy can lead to twin annihilation[28]. Thus, precise control of particle energy is essential to achieve a high density of twins. In conventional PVD techniques, the ionization of the plasma is typically around 10%, while advanced methods like arc ion plating or HiPIMS achieve 70%-90% ionization[29]. Additionally, the energy of the atoms in these techniques usually does not exceed 30 eV[30] and it cannot be adjusted through bias control[29], making precise ion energy control difficult. In this study, we combined HiPIMS with electromagnetic screening technology (Supplementary Fig. 1), ensuring that all Cr particles generated from the Cr target discharges are ions. These ions were uniformly accelerated to approximately 100 eV using a bias of 100 V[18]. This homogeneous ion energy effectively overcomes the energy barrier for twin formation, enabling the generation of high-density nanotwins.

The twin structures were further observed by HR-TEM and HAADF-STEM (Fig. 2). Different from metals/alloys with similar elemental or atomic sizes[31], the TBs in CrN are observed from two different locations along the Cr-{111} and N-{111} axes, denoted as Cr-TB and N-TB, respectively. According to the schematic diagram of the Cr-TB and N-TB twin boundaries (Supplementary Fig. 7), the twin boundaries shown in Fig. 2b are centered at Cr-{111} axes, which corresponds to Cr-TB. Meanwhile, the TBs depicted in Fig. 2c are located between two Cr-{111} axes and should be N-TB. The Helmholtz free energies of Cr-TB and N-TB are −10.342 and −10.400 eV/atom (Supplementary Fig. 7), respectively, with a minimal difference of 0.6%. Consequently, under sufficiently high energy conditions, both types of twins can grow and coexist in the coating. In addition to nanotwins, some single atomic layer mirror-symmetric structures (Fig. 2d) and large twins with dimensions ranging from 8 to 18 nm (Fig. 2e) are observed. The former exhibits elongated diffraction spots in the corresponding FFT, indicative of a precursor to twinning (Fig. 2d)[31], while the latter, in the case of twins, involves an expanded TB rather than a single atomic layer. The corresponding FFT reveals diffraction spots at 1/3 and 2/3{111} in the diffraction symmetry axis. HR-TEM shows the extended TB (Fig. 2f), demonstrating a distinct periodic structural feature, namely, SF occurring at every three {111} planes (indicated by white arrows). This characteristic aligns with the typical features of the 9 R phase[31,32], suggesting that the extended region is composed of the 9 R phase.

The nanohardness of NT-CrN determined by nanoindentation is remarkably high (approximately 36 GPa) compared to single-crystal CrN (22.5 ± 1.0 GPa), polycrystalline CrN (16-24 GPa), and nanocrystalline CrN (24-28 GPa) as displayed in Supplementary Fig. 8. At the same time, the elastic modulus of NT-CrN is only 319.0 GPa, and H/E and H^3/E^2 are 0.112 and 0.458, respectively, indicating concurrent toughness (Supplementary Fig. 8). Several micro-pillars are dug out from the NT-CrN coating by focused ion beam (FIB) techniques for the compression experiments. To prevent bending during compression, the ratio of the pillar height to diameter is set to be between 2 and 3[33]. The top diameter of the pillars is 300 nm and the initial height is 700 ± 60 nm. The compression distances are 10%, 20%, 30%, and 40% of the pillar height. The morphologies and stress-strain curves are displayed in Fig. 3a and Supplementary Fig. 9, respectively. Upon application of the load, the micro-pillars are gradually compressed from the top. Due to the conical shape of the pillar, no significant upsetting occurs when compression is less than 20%. As compression increases beyond 30%, evident upsetting occurs as manifested by a flattened pillar top, and the cross-sectional area of the flattened top increases with compression. The NT-CrN micro-pillar does not undergo brittle fracture during deformation like traditional ceramics but instead, it exhibits plastic deformation similar to metals at room temperature. However, in contrast to metals where deformation often manifests as overall pillar upsetting, the NT-CrN micro-pillar only shows top upsetting. The engineering stress-strain curve corresponding to the compression experiment is depicted in Fig. 3b. For strain less than 6%, stress increases linearly with strain, indicating elastic deformation, and the elastic limit is 10 GPa. When strain is larger than 6%, stress increases nonlinearly signifying plastic deformation. Therefore, the yield strength is approximately 10 GPa at the strain of 6%. Stress reaches a failure value of approximately 32 GPa at strain of 41%, following by a gradual decline until unloading commences at strain of 44.3%. After unloading, a certain degree of elastic recovery takes place and deformation stabilizes at approximately 37.3%. Compression is also conducted on more pillars with diameters of 400 nm and 500 nm and the strain and ultimate strength are 38%, 34%, and 33 GPa, 31 GPa,

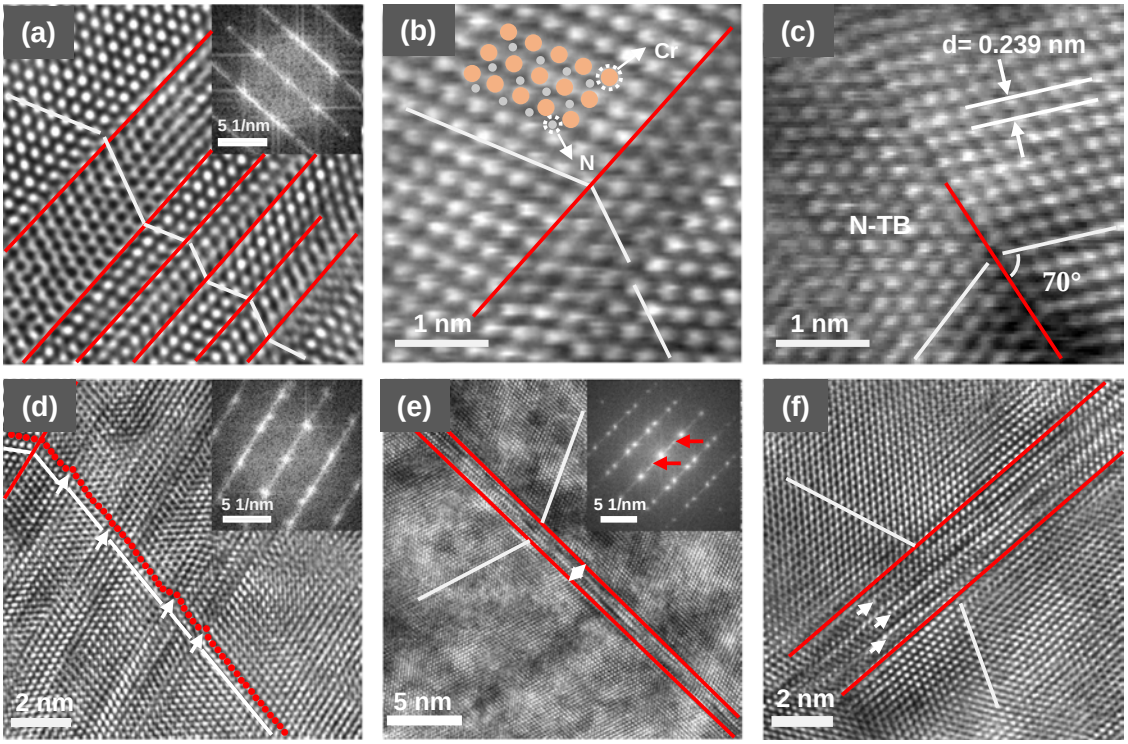

Fig. 2 | Twin structures in the CrN. a Typical twin structure with twin boundaries (TBs) marked by red solid lines and crystal planes by white solid lines. The inset shows the corresponding Fast Fourier Transform (FFT). **b**, **c** Are TBs with Cr-{111} (Cr-TB) and N-{111} (N-TB) as interfaces observed by HAADF-STEM, respectively. Based on the actual structure of CrN, the distribution of Cr and N atoms is shown in the inset of Fig. 2b (yellow markers for Cr and gray markers for N, located between Cr atoms). Therefore, the twin boundary (TB) shown in Fig. 2c is considered to be between the Cr-{111} planes, and it is assumed to be in the N-{111} planes. **d** Stacking fault (SF) is indicated by white arrows, which can also be considered as a twin with a single atomic layer thickness. **e** Twin with a large thickness, where the TB is the region between the red solid lines indicated by white double arrows. The inset shows the corresponding FFT, and the red arrows indicate the presence of 1/3 and 2/3{111} diffraction spots in the diffraction axis. **f** Extended TB shown in (**e**), where there is one SF between every three {111} planes, i.e., the 9 R phase, indicated by white arrows.

respectively (Supplementary Fig. 10), thus showing similar strength and plastic deformation capability.

Transforming the engineering stress-strain curve into the true stress-strain curve and strain strengthening rate reveals similar trends. Similar to the engineering stress-strain curve, the true stress exhibits linear increase at strain below 6%. Beyond 6% and up to 39% strain, the true stress shows nonlinear increase, followed by a gradual decline thereafter. The strain strengthening rate is positive at strain below 39% and becomes negative beyond 39%. The micro-pillars exhibit continuous strain strengthening throughout strain below 39%. The sustained strain strengthening in NT-CrN not only shows the plastic deformation capability exceeding 40%, but also failure strength exceeds 32 GPa.

Generally, metals exhibit greater ductility, but stress is typically less than 5 GPa, displaying characteristics of low strength and high ductility (Fig. 3c and Supplementary Table 2). In contrast, the ultimate strength of ceramic materials (TMC, TMB, TMN, TMO) is typically between 5 and 20 GPa with strain below 10%. Recently reported nanocrystalline diamond and c-BN materials have stress up to 170 GPa with strain exceeding 12%[34,35], which still exhibit characteristics of high strength and low ductility as ceramic materials. High strength and deformation capability have been reported for single crystals of TaC, ZrC, and ZrO_2 under compression along specific slip systems[36–38]. For polycrystalline TaCN, while good deformation capability has been observed during micropillar compression, brittle fracture remains predominant, and their toughness is still characteristic of ceramic materials[39]. In this study, by introducing high-density twins during sample growth, we successfully achieved room-temperature plastic deformation and recorded the highest strength for nanotwinned CrN. The toughness of NT-CrN was also assessed by indentation testing[40], as shown in Supplementary Fig. 11. In traditional CrN ceramic thin films, significant crack propagation typically occurs under loads less than 100 mN[41,42]. However, no cracks were observed at the apex of the indentation, indicating much better toughness. The amalgamation of high strength and high deformability in NT-CrN undoubtedly holds significant potential for engineering applications.

To investigate the continuous strengthening mechanism, the microstructures corresponding to points A, B, C, and D (In Fig. 3b) are shown in Supplementary Fig. 12. With increasing strain, NT-CrN initially exhibits stacking faults around the twin boundaries (Point A, Supplementary Fig. 12a), which are primarily attributed to the nucleation and glide of partial dislocations[10]. The twin boundaries act as effective barriers to dislocation motion, thereby contributing to early-stage strengthening[43]. As the applied load increases further, the twin width decreases and the structure gradually evolves into one characterized by a high density of stacking faults with diversified orientations (Point B, Supplementary Fig. 12b). Huang Y. et al.[44] have reported that an increase in stacking fault density leads to enhanced material strength; accordingly, the increased stacking fault density at Point B results in further strengthening. With additional strain, the stacking fault density starts to decline while a significant number of dislocations accumulate near the grain boundaries (Point C, Supplementary Fig. 12c). Upon further deformation, the intragranular stacking faults gradually disappear and dislocation pile-ups form at the grain boundaries (Point D, Supplementary Fig. 12d), which could further contribute to material strengthening by generating localized stress concentrations[45]. Although these microstructural evolutions continuously enhance the

https://doi.org/10.1038/s41467-025-61275-2

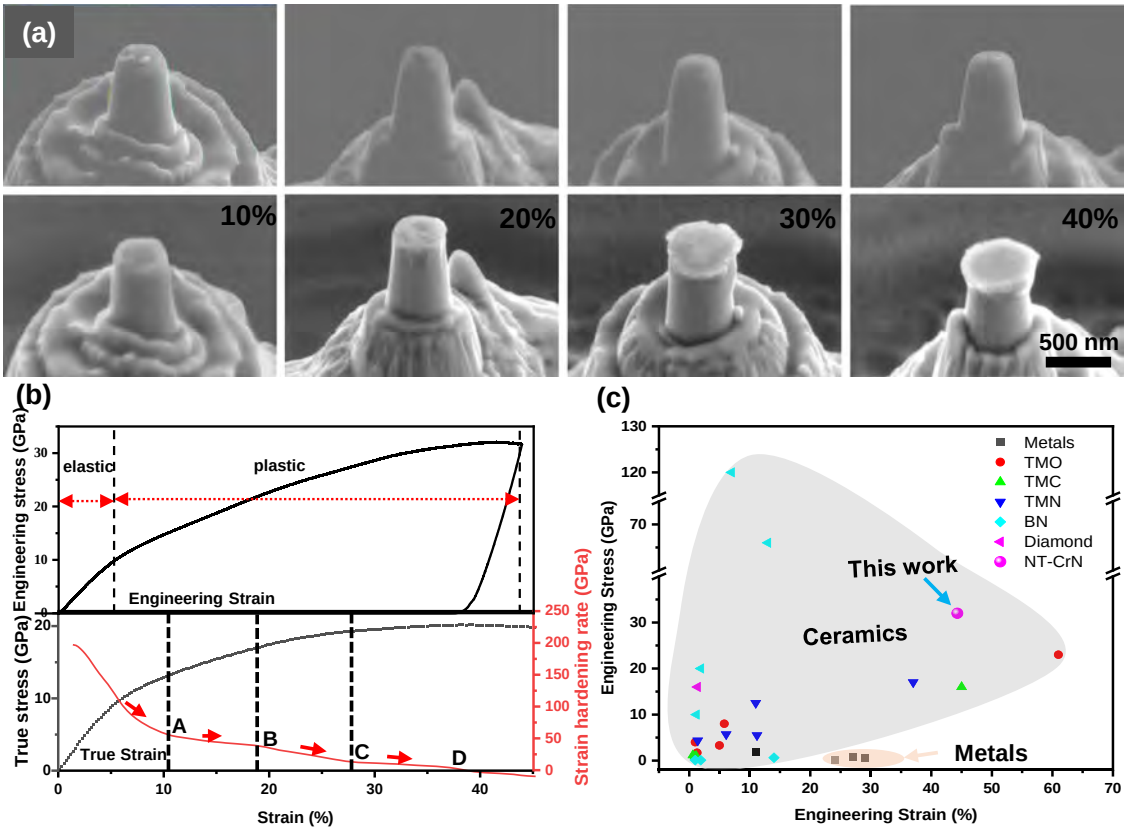

Fig. 3 | Mechanical properties of nano-twinned CrN (NT-CrN). a SEM images of NT-CrN micro-pillars before and after compression. The micro-pillar top diameter is 300 nm, height is 700 ± 60 nm, and cone angle is approximately 7.5°. The strain values correspond to 10%, 20%, 30%, and 40% of the micro-pillars' height. **b** Engineering stress-strain curve, corresponding true stress-strain curve, and strain hardening rate curve obtained from the true stress-strain curve. The yield strength is approximately 32 GPa at an engineering strain of about 41%, and strength begins to decrease slightly at a strain of 43%. There are four inflection points in the strain hardening rate curve denoted as A to D based on different slopes. Source data are provided as a Source Data file. **c** Engineering stress-strain comparison with typical engineering materials showing that NT-CrN exhibits both high strength and high ductility. Detailed data are shown in Supplementary Table 2[13,34,36–39,59–73].

strength of CrN, the observed decrease in defect density and the increase in grain size (Supplementary Fig. 13) with increasing strain lead to a reduction in the degree of strengthening. This overall trend is also reflected in the stress–strain curve, where the strain hardening rate decreases gradually.

Furthermore, compression tests on micropillars with varying twin boundary densities show that as the twin boundary density increases from 1.8×10^{11} to 3.1×10^{15} m^{-2}, the strength of CrN increases from 16.5 to 22.4 and 24.8 GPa(Supplementary Fig. 14). Therefore, it can be inferred that the overall strengthening of NT-CrN is closely related to the presence and evolution of twin boundaries. To detailly study the strengthening effect of the nano-twined CrN, we further calculated the elastic constants and the density of states (DOS). The calculated shear modulus (G) of nano-twinned CrN further supports the strengthening effect compared to single-crystal CrN. As listed in Supplementary Table 3, the G value of single-crystal CrN is 60.91 GPa, while CrN with Cr or N {111}-twinned boundaries exhibits G values of 159.44 and 185.83 GPa, respectively. Additionally, the mechanical properties of nano-twinned CrN with 2% nitrogen vacancies were also evaluated (In Supplementary Table 3), and the results show that little effect occur on the elastic constants compared to the strengthening effect provided by the twinned structure. Furthermore, the density of states at the Fermi level ($N(E_f)$) of twinned CrN with {111}Cr-TB and {111}N-TB is lower than that of single-crystal CrN (Supplementary Fig. 15). Indeed, a lower $N(E_f)$ correlates with enhanced crystal stability, thereby contributing to the intrinsic strength of the material[46]. Hence, our result indicates improved structural stability and enhanced mechanical strength of twinned CrN.

However, the observed $N(E_f)$ does not suggest an intrinsic enhancement in ductility which is directly related to the observed strong plasticity in the nano-twined CrN samples. Therefore, the twin boundary evolution during deformation was detailly studied, as shown in Fig. 4 (three positions with different deformation are selected from the top of the micropillar). Figure 4a shows the structures at small deformation, where there are numerous nanotwins and SF structures in the grains compared to those before deformation. Some TBs experience fracture and proliferation, resulting in certain steps at the fracture site with a height of several atomic layers. The breakage of TBs leads to a reduction in length and an increase in density, but the overall length remains relatively constant. The inset indicates that the height of the steps is different. Some interruptions occur between Cr-TB and N-TB with a height of 0.5 d{111} (D1), and some interruptions are found between N-TB and N-TB with a height of d{111} (D2). Multiple steps with larger heights are also present, likely formed by superposition of D1 and D2. By utilizing the Burgers circuit calibration method, 1/6 < 121> dislocations are discovered from the interruption sites of TBs. In metallic materials, such dislocations arise from the breakdown of pre-existing full dislocations induced by the interactions with TBs during deformation (e.g., $1/2[101] \rightarrow 1/3[111] + 1/6[12\bar{1}]$)[33]. However, in ceramic materials, the movement of atoms from one equilibrium position to another (1/2 < 121> displacement) requires a higher energy, making such interactions almost improbable. Interestingly, Yadav, S. K. et al. have found from first-principles calculation that in transition metal nitrides with TiN as an example, due to the alternating distribution of Ti and N, and both being potential TBs, Ti and N can move 1/6 < 121> to the opposite directions (0.5 d{111}) to achieve fracture of the TB[47]. This

https://doi.org/10.1038/s41467-025-61275-2

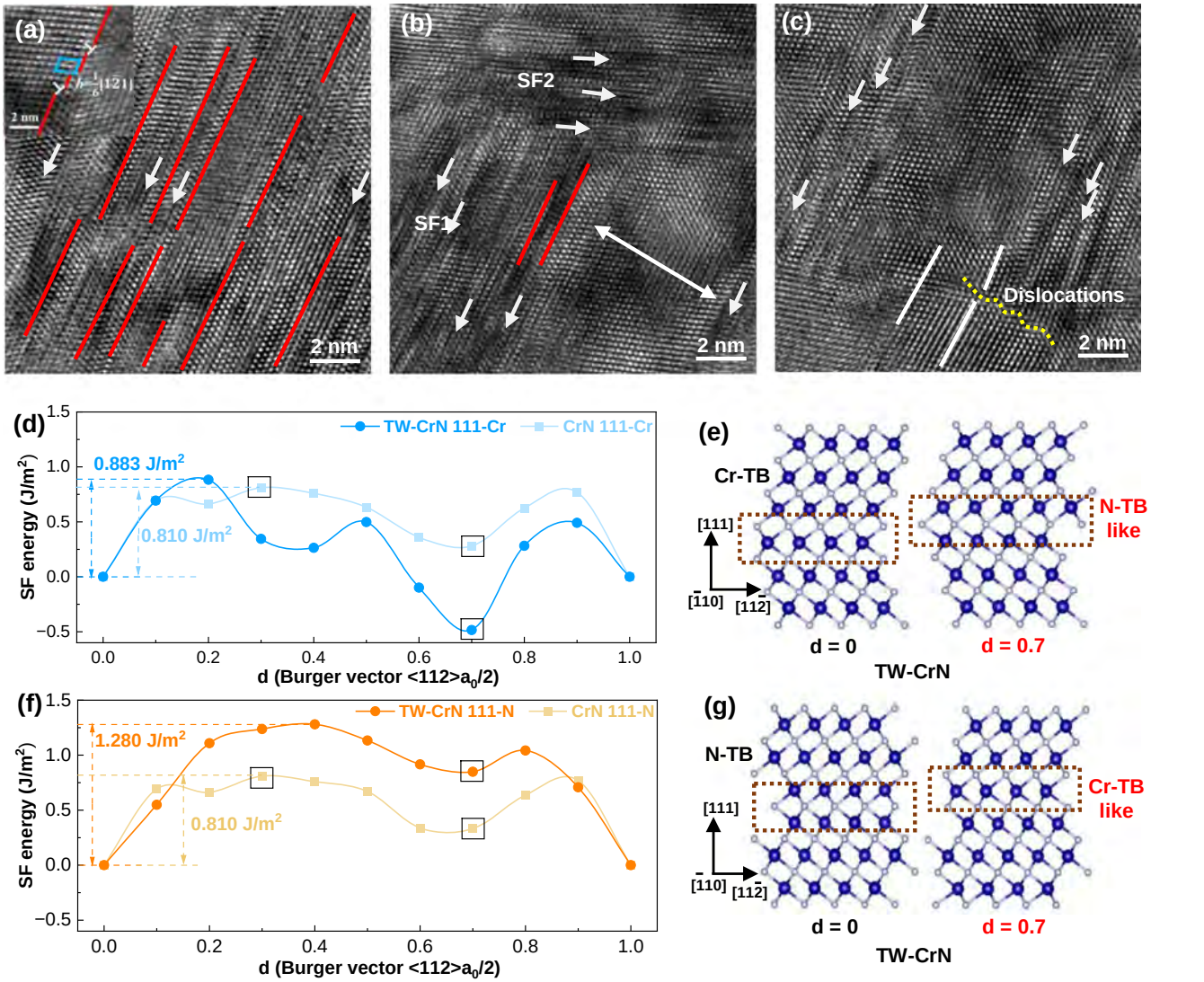

Fig. 4 | Microscopic morphology of NT-CrN at different deformation levels. **a** Structures at small deformation, TBs break with numerous twins and SFs. The inset shows two types of steps at the TB break, one with a height of 0.5 d{111} and the other with a height of d{111}. A 1/6[12$\bar{1}$] partial dislocation at the step (red solid line represents TB, white arrows represent SF, white T represents dislocation, blue line frame represents a Burgers circuit, and white solid line represents symmetric crystal planes on both sides of TB). **b** With increasing deformation, the structure shows a reduced number of TBs and the emergence of large areas with a regular atomic arrangement (indicated by white double arrows). Two types of SF (indicated by white arrows) are present, one parallel to TB and the other inclined to TB. **c** At high deformation, only SF and dislocation walls (indicated by yellow dashed lines) were observed. **d**–**g** First-principles calculations, (**d**) SF energy changes for Cr-TB and CrN single crystal with Cr(111) as the slip plane at different sliding distances; (**e**) the initial and deformed structures of Cr-TB at the sliding distance of 0.7 d; (**f**) SF energy changes for N-TB and CrN single crystal with N(111) as the slip plane at different sliding distances; (**g**) Initial and deformed structures of N-TB at the sliding distance of 0.7 d.(Source data are provided as a Source Data file).

significant reduction in the distance greatly decreases the energy barrier for the interactions between dislocations and TBs. Consequently, dislocations move laterally relative to the TBs, leading to TB fracture. This is consistent with the presence of Cr-TB and N-TB in CrN. After the partial dislocation is generated, it slides along the TB based on the same mechanism, resulting in the transition of the TB (D1-type interruptions). At the positions with higher strain energy, dislocations continue to fracture TBs in the same manner, generating multi-step lateral movements. Subsequently, they collectively slide along the TB, leading to the D2-type interruptions or even taller interruptions among the TBs.

Figure 4b shows that the TBs number in the grain decreases significantly with larger deformation, giving rise to larger areas of atomically regular arrangements. This indicates that a certain degree of detwinning occurs. SFs emerge near the TBs. Some SFs (SF1) are parallel to the TB, while others (SF2) are mainly distributed at the ends of the TBs at an angle of about 72° with the TB. In the process of detwinning in metals, dislocations generated after TB interruption will continue to glide along the TB toward its ends. This results in the overall translation of the TB between atomic layers. When it reaches a position coincident with another TB, merging of twins and completion of the detwinning process occur. Previous studies indicate that the collective glide of multiple partial dislocations can reduce the stress required for atomic rearrangement[46]. For example, in the FCC structure, when the vector sum of three 1/6 < 121> dislocations is equal to zero (e.g., 1/6[12$\bar{1}$], 1/6 [$\bar{1}\bar{1}$2], and 1/6[$\bar{1}$2$\bar{1}$]), it requires less force for atomic rearrangement than three single-direction 1/6 < 121> dislocations[48,49]. The preferential slip along TBs is often inclined toward a collective slip of three atomic layers. When the number of adjacent atomic layers is a multiple of three, the two TBs will coincide after translation, leading to detwinning. However, when the number of adjacent atomic layers is not a multiple of three, the two TBs slide to a

separation of 1-2 atomic layers forming a SF referred to as SF1. At the same time, when the interruption height between TBs is relatively large, there will be more atomic layers between the two TBs. This produces an energy increase at the interruption site[50]. To minimize the energy, new partial dislocations will form at the interruption site[51], and these dislocations will have a 72° angle with the TBs, ultimately giving rise to secondary SF, denoted as SF2. It is evident that a similar detwinning process occurs in the CrN twins (Supplementary Fig. 16). The distinction lies in the activation of dislocation slip, which initiates from a smaller distance between Cr and N and continues with the same displacement, leading to twin merging and new SF formation.

As deformation increases further, the TBs and SF1 formed during the detwinning almost disappear, with only a small number of SF2 is retained. Some dislocation walls formed by the accumulation of dislocations is evident (Fig. 4c), indicating that the detwinning process is completed. Similar to metals, dislocation walls are the products of TBs annihilation. SF1 formed by the translation of TBs interact with dislocations once again. Eventually, SF1 disappears and results in a regularly arranged lattice. Due to the different orientation of SF2 compared to the TB, nearby dislocations must undergo lateral movement firstly before engaging in slipping along the SF. Hence, a small quantity of SF2 persists in the grain. Ultimately, the majority of SF2 disappears, accompanied by a noticeable increase in the grain size (Supplementary Fig. 13), marking the completion of detwinning. However, dislocation walls still persist in the grain since there is no TB in CrN ceramics to facilitate their propagation and movement. They remain stationary and ultimately, become the origin of crack initiation during further deformation.

In general, ceramics characterized by covalent or ionic bonds cannot slip at room temperature (a key factor in determining their plasticity). The deformation at room temperature primarily arises from changes in atomic distances caused by the stretching and compression of these bonds. Some special ceramic materials have also been reported to exhibit plastic deformation capabilities. For example, Mo/La_2O_3 relies on the dislocation generation in the metallic layers to facilitate dislocation motion within the ceramic[12], thereby enabling deformation. Specific structures, such as twisted-layer configurations, were employed to reduce the interlayer sliding energy in van der Waals materials[13], promoting slip and deformation. However, these types of ceramic materials generally exhibit relatively low strength. Previous studies have demonstrated how specific crystallographic orientations or material alloying strategies can enable significant plastic deformation of ceramic materials at room temperature[34–37]. These works emphasize the role of twin boundaries, dislocations, and stacking faults in strengthening these materials. To investigate the slip mechanism in NT-CrN, we compute the generalized SF energies of single crystal CrN and NT-CrN unit cells along the [112] slip direction in the (111) plane by first-principles, as depicted in Fig. 4d, e. For single crystal CrN, when Cr(111) or N(111) plane is the slip plane, moving the upper half of the structure along the [112] direction in 10 steps to the next equivalent symmetric position requires energy barriers of 0.810 and 0.810 J/m^2, respectively. These values are smaller than those of TiN (1.46 J/m^2), ZrN (1.46 J/m^2), and HfN (1.52 J/m^2) but comparable to those of VN (0.62 J/m^2), NbN (0.67 J/m^2), and TaN (0.63 J/m^2)[52]. Although there are low-energy positions during the slip process such as Cr-0.2 d, Cr-0.7 d, N-0.2 d, or N-0.7 d, their energies are higher than the initial position. Therefore, the crystallographic axes of Cr or N are unlikely to undergo slip. If slip occurs, it is prone to bonding breakage, forming hexagonal rings leading to eventual fracture while precluding plastic deformation as displayed in Supplementary Fig. 17. In the presence of nanotwins, either the Cr(111) twin plane or N(111) twin plane is the slip plane, moving the upper half of the structure along the [112] direction through the same slipping process requires energy barriers of 0.883 and 1.280 J/m^2, respectively. These values are greater than the maximum generalized SF energy that needs to be overcome during slipping in single crystals. Particularly, it is more challenging to induce slipping, especially for N(111) twin planes as the slip plane. In addition, when nanotwin boundaries exist in Cr-{111}, a much smaller energy (far below the initial energy) at Cr-0.7 d occurs during the slip process. Based on the four-sided structure formed by the TB and adjacent atoms, Cr-0.7 d is just the location of the nanotwin boundary at N-{111}. This implies that at a certain external energy, the transformation of the nanotwin boundary from Cr-{111} to N-{111} is possible, which is different from nano-twinned metals. In metallic materials, twin boundaries are relatively simple structures consisting solely of metal atoms. In the case of nanotwinned CrN, the grain boundaries are composed of both Cr-TB and N-TB twin boundaries. While the strengthening effect is similar to that observed in metallic twins, the sliding mechanism between Cr-TB and N-TB is different. Specifically, the slip of N-TB requires much higher energy, resulting in a significantly stronger strengthening effect. Besides, the most important discovery from the crystal structure diagrams is that the four-sided structure formed by Cr-TB and adjacent atoms with two Cr atoms as vertices evolves into a quadrilateral formed by N-TB and adjacent atoms with two N atoms as vertices, and no hexagonal ring resulting from bonding breakage occur during the process, which is different to the single CrN crystal as shown in Supplementary Fig. 17. This shows that slipping of NT-CrN is attributed to twisting of a polyhedron constructed by nano-TB without bonding breakage, and based on this special slipping, room-temperature plasticity is obtained in NT-CrN.

As stated above, the deformation behavior at the top of the micropillars shows a top upsetting phenomenon, which could also be explained by the detwinning process. When the load is initially applied, the stress at the top of the micron-pillar is higher than in other regions, causing the top to undergo a transformation from Cr-TB to N-TB and a detwinning process, accompanied by plastic deformation. Once detwinning is complete, the top of the micron-pillar restores the high crystal-quality structure, resembling the behavior observed in traditional ceramics, with cracks forming at the periphery. Meanwhile, due to the lower stress at the bottom and the high hardness of nanotwinned CrN, which provides sufficient support to resist deformation, the deformation at the bottom is smaller than at the top. As a result, the micron-pillar exhibits top upsetting and crack formation.

However, in previous research[53], researchers reported that detwinning is difficult in covalent materials like diamond and cubic boron nitride. To reveal the ease of detwinning, the energies for the slip of dislocation near the twin boundary and away from the twin boundary was calculated. For purely covalent ceramics such as diamond and cubic boron nitride, these two energies are comparable[54]. In other words, since the energy required for dislocation glide along the twin boundary is equivalent to that on other slip planes away from the twin boundary, twin boundaries do not migrate easily, leading to a stable structure. However, it is founded the energy barrier of dislocation slip near the twin boundary is lower than away from the twin boundary in NT-CrN (Supplementary Fig. 18), resembling the behavior of metals[54], which facilitates the ease of detwinning.

In summary, controlled growth of CrN structures is realized by adjusting the ion kinetic energy, and nanotwin CrN with a density of 9.0×10^{15} m^{-2} and twin-containing grain volume fraction of about 52 % is prepared. The nanotwins have an average thickness of 3.8 nm, and TBs are distributed in both the Cr-{111} and N-{111} axes. NT-CrN exhibits not only super high hardness (>36 GPa) but also room-temperature plasticity. It can tolerate compression deformation of over 40% without brittle failure. The room temperature plasticity contributes to the distribution of nanotwin boundaries consequently allowing special slipping by twisting of the polyhedron constructed by nano-TB without bonding breakage. This leads to energy absorption by twin proliferation and fusion in the detwinning process and fracture and failure occur only at the extensive dislocation walls formed after detwinning.

Methods

The CrN coatings were deposited on (100) Si wafers, high-speed steel (HSS, φ30 × 3 mm) substrates and insulating soda-lime glass substrates. The HSS substrates were polished with SiC sandpaper from 320 to 1500 grit and polished with velvet cloth and 1 μm diamond paste. The substrates were cleaned ultrasonically for 15 minutes in alcohol and acetone, dried for 5 minutes by heating, and fixed in a sample holder. The coating was deposited in a vacuum chamber with dimensions of 600 mm × 600 mm × 500 mm and at a base pressure of 5.0×10^{-3} Pa. A custom-designed cylindrical sputtering cathode shown in Supplementary Fig. 1 equipped with a Melec GmbH high-power impulse magnetron sputtering power supply was used. The deposition process described in Supplementary Fig. 19 comprised three main stages, cleaning, transition layer deposition, and coating deposition. During the cleaning process, 10 sccm Ar (purity 99.99%) was introduced to a working pressure of 1.0 Pa. The Ar flow rate was increased to 40 sccm at a rate of 1 sccm/10 s. The substrate was biased at −650 V and cleaning was performed at 100 W and 2.0 kW for 10 and 8 minutes, respectively. The voltage was then reduced to −100 V and the Ar flow rate was reduced to 10 sccm. In the transition layer deposition process, the N_2 flow rate was increased to 11 sccm at a rate of 30 s/sccm. Finally, the CrN coatings were deposited for 20 minutes at 3.5 kW (frequency of 50 Hz, pulse width of 300 μs). The substrate temperature was monitored throughout the process by a thermocouple (WRNK-191, ChenYi Instrument, China), and the temperature variation is shown in Supplementary Fig. 19.

The structural characteristics of the CrN coating, such as the crystal orientation and grain size, were determined by X-ray diffraction (D8 Advance, Bruker, Germany) in θ−2θ mode. The thickness, surface morphology, and interface characteristics of the CrN coating were examined by field-emission scanning electron microscopy (FE-SEM, SUPRA@55, Carl Zeiss, Germany). Transmission electron microscopy (TEM) and high-resolution TEM (HRTEM) (JEM-3200FS, JEOL, Japan) were employed to study the microscopic structure of CrN and the variations in microstructure, such as twinning and SFs, at different deformation levels. The nanotwin structure was confirmed and analyzed using high-angle annular dark field scanning transmission electron microscopy (HAADF-STEM). The TEM samples were prepared by a focused ion beam (FIB, Scios, FEI, USA) using a gradually reduced energy Ga ion beam to preserve the original features. The resistivity of NT-CrN on glass substrates was measured using a Hall effect measurement system (Hall8800, Precision Systems Industrial Limited). Measurements were conducted at five randomly selected regions, and the results were averaged.

The micro-pillar samples with diameters of 300, 400, and 500 nm were prepared by a focused ion beam (FIB, Scios, FEI, USA). The cone angle of the pillars was set at 5° and the length-to-width ratios (diameter: height) between 1:2 and 1:3 to minimize the lateral constraints. To minimize the influence of the substrate during micro-pillar preparation, the height of the micro-pillars did not exceed one-third of the coating thickness. In order to reduce milling damage, the micro-pillars were finely polished with ion beams at 5 kV, 87 pA, and 2 kV (7 pA after initial milling at 30 kV and 1 nA). The hardness and strength were measured on a nanoindenter (Nano Indenter G200, Agilent Technologies, USA) with Berkovich tips under a maximum load of 10 mN. To minimize errors, the indentation depth during the hardness test was kept below 1/10 of the film thickness. Fracture toughness was evaluated using nanoindentation (Fischerscope HM2000) under applied loads of 100 mN and 500 mN, using a Berkovich indenter. During the strength test, the micro-pillars were compressed at a rate of 2 nm/s, which corresponded to a strain rate of $2.5\text{-}3.0 \times 10^{-3}$/s. The load, displacement and time data were recorded at 500 Hz. The compressive strength (σ) was calculated as σ = F/A, where F is the applied force and A is the cross-sectional area of the nanocolumn.

We constructed single-crystal CrN and twin CrN cells with crystallographic axes [11$\bar{2}$], [1$\bar{1}$0], and [111], each containing 24 atoms and structural optimization of these two samples by the Vienna Ab Initio Simulation Package (VASP) code[55], periodic boundary conditions, projector-augmented wave (PAW) potentials[56], and Perdew-Burke-Ernzerhof (PBE) generalized gradient approximation[57]. The atomic positions and structural parameters were relaxed by the conjugate gradient optimization method, with the total energy of the structure converging to 10^{-6} eV/atom and residual forces on each atom less than 0.005 eV/Å. For structural optimization, an 8 × 8 × 2 Monkhorst-Pack k-point grid and 500 eV cut-off energy were used. After structural relaxation, each sample had the (111) glide plane selection, and the entire structure above the slip plane was shifted to the equivalent symmetric position 10 times along the [112] direction. During structural optimization of the model after each slip, the atoms were constrained to relax only in the direction perpendicular to the slip plane. A 15 Å vacuum gap was used to establish free surfaces and break the periodicity in the [111]-direction. The total energy of each structure was then calculated after the completion of structural optimization. The generalized SF energy (GSFE) is computed using the following formula[52].

$$E_{GSFE} = (E_f - E_0)/S \quad (1)$$

where the E_{GSFE} is the generalized SF energy, E_f and E_0 are the total energies of the structure before and after slip, respectively, and S is the area of the glide plane.

To evaluate the strengthening effect of twinned boundaries on CrN's mechanical properties and explore the influence of N vacancies, we expanded the 24-atom cell of nano-twinned CrN along the [1$\bar{1}$0] axis to obtain a 48-atom cell for elastic parameter calculations. One N atom was removed in the 48-atom cell to simulate the vacancy effect. The elastic constants of single-crystal CrN were also computed for comparison. Small finite distortions were applied to the lattice vectors to obtain the elastic tensor, while polycrystalline bulk modulus (B), shear modulus (G), and elastic modulus (E) were derived using the Voigt-Reuss-Hill approximation.

Data availability

The source data generated in this study have been deposited in the Figshare database (https://doi.org/10.6084/m9.figshare.29091080)[58]. Source data are provided with this paper.

References

1. Karch, J. et al. Ceramics ductile at low temperature. *Nature* **330**, 556–558 (1987).
2. Zhang, J. et al. Plastic deformation in silicon nitride ceramics via bond switching at coherent interfaces. *Science* **378**, 371–376 (2022).
3. Wilkerson, R. P. et al. A novel approach to developing biomimetic ("nacre-like") metal-compliant-phase (nickel-alumina) ceramics through coextrusion. *Adv. Mater.* **28**, 10061–10067 (2016).
4. Guo, S. Q. et al. Tough hybrid ceramic-based material with high strength. *Scr. Mater.* **67**, (2012).
5. Krishnamurthy, R. et al. Experimental observations of high fracture resistances in SiC/$A1_2O_3$ laminated composites. *J. Am. Ceram. Soc.* **84**, 2451–2453 (2001).
6. Takei, T. et al. Thermal expansion behavior of particulate-filled composites I: Single reinforcing phase. *Mater. Sci. Eng. A* **131**, 133–143 (1991).
7. Peigney, A. et al. Tougher ceramics with nanotubes. *Nat. Mater.* **2**, 15–16 (2003).
8. Porz, L. et al. Dislocation-toughened ceramics. *Mater. Horiz.* **8**, 1528–1537 (2021).

9. Yi, H. et al. Ultra-dense dislocations stabilized in high entropy oxide ceramics. *Nat. Commun.* **13**, 2871 (2022).
10. Tian, Y. et al. Ultrahard nanotwinned cubic boron nitride. *Nature* **493**, 385–388 (2013).
11. Huang, Q. et al. Nanotwinned diamond with unprecedented hardness and stability. *Nature* **510**, 250–253 (2014).
12. Dong, L. R. et al. Borrowed dislocations for ductility in ceramics. *Science* **385**, 422–427 (2024).
13. Wu, Y. J. et al. Twisted-layer boron nitride ceramic with high deformability and strength. *Nature* **626**, 779–784 (2024).
14. Zhang, Y. et al. Elastic properties and stacking fault energies of borides, Carbides and Nitrides from First-Principles Calculations. *Acta Metall. Sin. (Engl. Lett.)* **32**, 1099–1110 (2019).
15. Li, X. Y. et al. Dislocation nucleation governed softening and maximum strength in nano-twinned metals. *Nature* **464**, 877–880 (2010).
16. Fang, T. H. et al. Revealing extraordinary intrinsic tensile plasticity in gradient nano-grained copper. *Science* **331**, 1587–1590 (2011).
17. Zhao, S. T. et al. Cryoforged nanotwinned titanium with ultrahigh strength and ductility. *Science* **373**, (2021).
18. Cui, S. H. et al. Hollow cathode effect modified time-dependent global model and high-power impulse magnetron sputtering discharge and transport in cylindrical cathode. *J. Appl. Phys.* **125**, 63302 (2019).
19. Lu, L. et al. Ultrahigh Strength and High Electrical Conductivity in Copper. *Science* **304**, 422–426 (2004).
20. Liao, C. Z. et al. Crystal Structures of Al-Nd Codoped Zirconolite Derived from Glass Matrix and Powder Sintering. *Inorg. Chem.* **54**, 7353–7361 (2015).
21. Zhu, J. et al. Microdiffraetion from Stacking Faults and Twin Boundaries in FCC Crystals. *J. Appl. Cryst.* **16**, 171–175 (1983).
22. Rauch, E. F. et al. Automated crystal orientation and phase mapping in TEM. *Mater. Charact.* **98**, 1–9 (2014).
23. Sun, Y. A. et al. Effects of stacking fault energy on deformation induced grain boundary relaxation in nanograined Cu alloys. *Acta Mater.* **239**, 118256 (2022).
24. An, X. H. et al. High strength and utilizable ductility of bulk ultrafine-grained Cu–Al alloys. *Appl. Phys. Lett.* **92**, 103 (2008).
25. Yang, S. et al. Nanotwinned transition metal nitride coating with excellent thermal stability. *Acta Mater.* **267**, 119743 (2024).
26. Yang, S. et al. High-density twin boundaries in transition metal nitride coating with boron doping. *Acta Mater.* **255**, 119033 (2023).
27. Rafailović, L. D. et al. High density of genuine growth twins in electrodeposited aluminum. *Sci. Adv.* **5**, eaax3894 (2019).
28. Chang, L. P. et al. Effect of substrate bias on the formation of nanotwin and properties in Cu thin films for advanced packaging technology. *Surf. Coat. Tech.* **482**, 130737 (2024).
29. Helmersson, U. et al. Ionized physical vapor deposition (IPVD): A review of technology and applications. *Thin Solid Films* **513**, 1–24 (2006).
30. Andritschky, M. et al. Energy deposition and substrate heating during magnetron sputtering. *Vacuum* **44**, 809–813 (1993).
31. Qiao, L. et al. Study on twin stacking faults in vaterite tablets of freshwater lacklustre pearls. *J. Cryst. Growth* **304**, 253–256 (2007).
32. Li, Q. et al. High-Strength Nanotwinned Al Alloys with 9R Phase. *Adv. Mater.* **30**, 1704629 (2018).
33. Wu, G. S. et al. Near-ideal strength and large compressive deformability of a nano-dual-phase glass-crystal alloy in sub-micron. *Scr. Mater.* **188**, 290–295 (2020).
34. Wheeler, J. M. et al. Approaching the Limits of Strength: Measuring the Uniaxial Compressive Strength of Diamond at Small Scales. *Nano Lett.* **16**, 812–816 (2016).
35. Zhao, S. J. et al. Mechanical properties of hybrid graphene and hexagonal boron nitride sheets as revealed by molecular dynamic simulations. *J. Phy. D: Appl. Phys.* **46**, 135303 (2013).
36. Kiani, S. et al. Nanomechanics of Refractory Transition-Metal Carbides: A Path to Discovering Plasticity in Hard Ceramics. *J. Am. Ceram. Soc.* **98**, 2313–2323 (2015).
37. Kiani, S. et al. In situ transmission electron microscopy observations of room-temperature plasticity in sub-micron-size TaC(100) and TaC(011) single crystals. *Scr. Mater.* **100**, 13–16 (2015).
38. Liang, C. Y. et al. Extreme dislocation-mediated plasticity of yttria-stabilized zirconia. *Mat. Today Phys.* **22**, 100588 (2022).
39. Glechner, T. et al. Assessment of ductile character in superhard Ta-C-N thin films. *Acta Mater.* **179**, 17–25 (2019).
40. Lawn, B. et al. Hardness, Toughness, and Brittleness: An Indentation Analysis. *J. Am. Ceram. Soc.* **62**, 347–350 (1979).
41. Wang, Q. et al. Evaluating mechanical properties and crack resistance of CrN, CrTiN, CrAlN and CrTiAlN coatings by nanoindentation and scratch tests. *Surf. Coat. Tech.* **285**, 203–213 (2016).
42. Shi, X. et al. Dynamic fracture of CrN coating by highly-resolved nano-impact. *Surf. Coat. Tech.* **383**, 125288 (2019).
43. Fu, T. et al. Effects of twin boundaries in vanadium nitride films subjected to tensile/compressive deformations. *Appl. Surf. Sci.* **426**, 262–270 (2017).
44. Huang, Y. et al. High density of stacking faults strengthened TaN/TiN multilayer. *Acta Mater.* **255**, 119027 (2023).
45. Zhang, J. et al. Impact of dislocation densities on the microscale strength of single-crystal strontium titanate. *Acta Mater.* **291**, 121004 (2025).
46. Dahlqvist, M. et al. Influence of boron vacancies on phase stability, bonding and structure of MB2 (M = Ti, Zr, Hf, V, Nb, Ta, Cr, Mo, W) with AlB2 type structure. *J. Phys.: Condens. Matter* **27**, 435702 (2015).
47. Yadav, S. K. et al. First-principles density functional theory study of generalized stacking faults in TiN and MgO. *Philos. Mag.* **94**, 464–475 (2014).
48. Wang, J. et al. Detwinning mechanisms for growth twins in face-centered cubic metals. *Acta Mater.* **58**, 2262–2270 (2010).
49. Cao, Y. et al. Grain boundary formation by remnant dislocations from the de-twinning of thin nano-twins. *Scr. Mater.* **100**, 98–101 (2015).
50. Li, N. et al. Quantification of dislocation nucleation stress in TiN through high-resolution in situ indentation experiments and first principles calculation. *Sci. Rep.* **5**, 15813 (2015).
51. Duan, F. H. et al. Ultrastrong nanotwinned pure nickel with extremely fine twin thickness. *Sci. Adv.* **7**, eabg5113 (2021).
52. Yu, H. et al. Understanding dislocation slip in stoichiometric rock-salt transition metal carbides and nitrides. *J. Mater. Sci.* **28**, 6235–6248 (2017).
53. Tong, K. et al. Structural transition and migration of incoherent twin boundary in diamond. *Nature* **626**, 79 (2024).
54. Wen, B. et al. Continuous strengthening in nanotwinned diamond. *Npj Computational Mater.* **5**, 117 (2019).
55. Kresse, G. et al. Efficiency of ab-initio total energy calculations for metals and semiconductors using a plane-wave basis set. *Comp. Mater. Sci.* **6**, 15–50 (1996).
56. Blöchl, P. E. et al. Projector augmented-wave method. *Phys. Rev. B* **50**, 17953 (1994).
57. Perdew, J. P. et al. Generalized gradient approximation made simple. *Phys. Rev. Lett.* **77**, 3865 (1996).
58. Liu, L. L. et al. Source data of Nanotwinned CrN ceramics with enhanced plasticity. Figshare, https://doi.org/10.6084/m9.figshare.29091080 (2025).
59. Xue, S. et al. High strength, deformable nanotwinned Al-Co alloys. *Mater. Res. Lett.* **7**, 33–39 (2019).
60. Yilmaz, H. et al. The size dependent strength of Fe, Nb and V micropillars at room and low temperature. *Materialia* **7**, 100424 (2019).
61. Jennings, A. T. et al. Higher compressive strengths and the Bauschinger effect in conformally passivated copper nanopillars. *Acta Mater.* **60**, 3444–3455 (2012).

62. Masuda, H. et al. Ferroelastic and plastic behaviors in pseudo-single crystal micropillars of nontransformable tetragonal zirconia. *Acta Mater.* **203**, 116471 (2021).
63. Sung, T. H. et al. Yielding and plastic slip in ZnO. *Appl. Phys. Lett.* **100**, 211903 (2012).
64. Matweb, Material property data, https://www.matweb.com/index.aspx (2022).
65. Tsai, J. F. et al. Transformation plasticity and toughening in CeO2-partially-stabilized zirconia–alumina (Ce-TZP/Al2O3) composites doped with MnO. *J. Am. Ceram. Soc.* **75**, 1229–1238 (1992).
66. Poon, B. et al. Damage accumulation and hysteretic behavior of MAX phase materials. *J. Mech. Phys. Solids* **59**, 2238–2257 (2011).
67. Benitez, R. et al. Mechanical properties and microstructure evolution of Ti2AlC under compression in 25-1100°C temperature range. *Acta Mater.* **189**, 154–165 (2020).
68. Hu, L. et al. High-performance metal/carbide composites with far-from-equilibrium compositions and controlled microstructures. *Sci. Rep.* **6**, 35523 (2016).
69. Subhash, G. et al. Mechanical behaviour of a hot-pressed aluminum nitride under uniaxial compression. *J. Mater. Sci.* **33**, 1933–1939 (1998).
70. Wheeler, J. M. et al. Extraction of plasticity parameters of GaN with high temperature, in situ micro-compression. *Int. J. Plasticity* **40**, 140–151 (2013).
71. Wheeler, J. M. et al. Deformation of hard coatings at elevated temperatures. *Surf. Coat. Tech.* **254**, 382–387 (2014).
72. Wu, Y. et al. The rise of plastic deformation in boron nitride ceramics. *Sci. China Mater.* **64**, 46–51 (2021).
73. Baily, S. The property data of "Diamond (C) - Properties and applications", AZoM, https://www.azom.com/article.aspx?ArticleID=262 (2001).

Acknowledgements

This work was financially supported by the National Key R&D Program of China (Grant No. 2023YFA1608802(Z. Wu) and 2023YFF0716800(K. Zhang)), National Natural Science Foundation of China (No. 52322206(K. Zhang) and No. 52305174(S. Cui)), 2022 Shenzhen sustainable supporting funds for colleges and universities (No.20220810143642004(Z. Wu)), Guangdong Natural Science Foundation(No.2025A1515010745(L. Liu)), China Postdoctoral Science Foundation(No.2024M750089(L. Liu)), Shenzhen postdoctoral research fund project after outbound (No. 2129933651(S. Cui)), Shenzhen-Hong Kong Research and Development Fund (No. SGDX20201103095406024(Z. Wu)), Guangdong - Hong Kong Technology Cooperation Funding Scheme (TCFS) (No. GHP/085/18SZ(P. Chu)).We also acknowledged the High-Performance Computing Center of Jilin University, China.

Author contributions

Z.W., S.C., and K.Z. conceived the study. L.L., X.A., T.L., and X.G. perform the experiment, collect the data, created all figures and wrote the first draft of the manuscript. D.Y., B.H., Q.X., Z.M., and S.C. assisted in data collection and analysis. X.T. and P.C. provided for many helpful discussions and advice in date analysis. All authors contributed to revisions and the final draft of this manuscript. L.L., X.A., X.G. and T.L. contributed equally to this work.

Competing interests

The authors declare no competing interests.

Additional information

Supplementary information The online version contains supplementary material available at https://doi.org/10.1038/s41467-025-61275-2.

Correspondence and requests for materials should be addressed to Kan Zhang, Suihan Cui or Zhongzhen Wu.

Peer review information *Nature Communications* thanks the anonymous reviewers for their contribution to the peer review of this work. A peer review file is available.

Supplementary Information

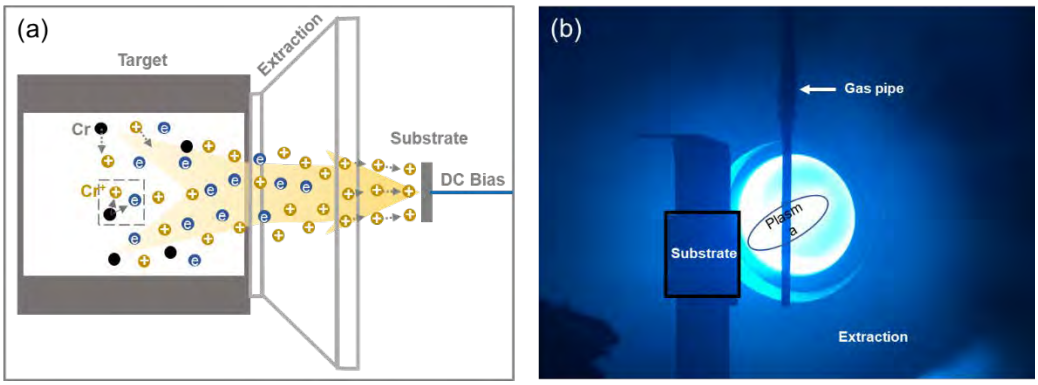

Supplementary Figure 1 Experiment equipment. (a) Schematic diagram of the cylindrical sputtering cathode including cathode and electromagnetic extraction system. The ions sputtered from the cathode are transported to the substrate by an electromagnetic extraction system and accelerated by the voltage applied to the sample for coating deposition. (b) Plasma discharge showing that the plasma accumulates in the central region of the cylindrical cathode.

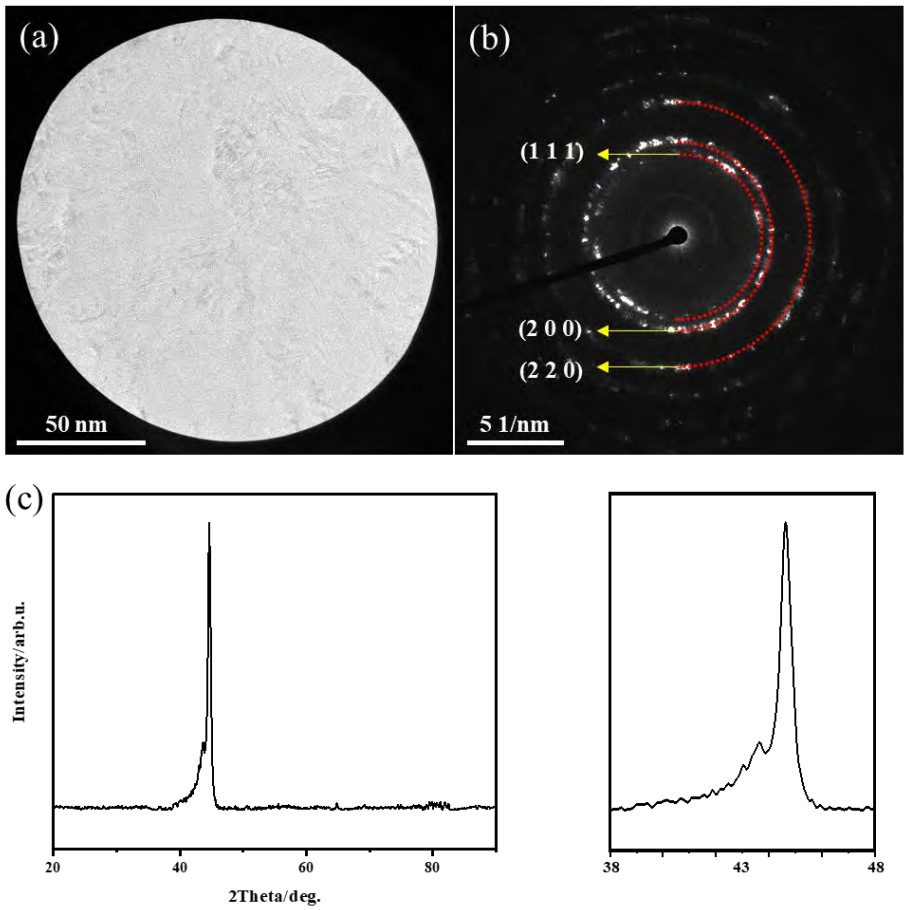

Supplementary Figure 2 Structural characteristics of CrN. (a) Electron diffraction region by TEM and (b) SAED pattern. The diffraction ring with the highest intensity corresponds to (200), followed by plane (111) and plane (220). (c) XRD pattern and magnification showing the strongest peak at 2θ = 44.3°, indicating that CrN has the (200) preferred orientation consistent with SAED. The difference is that no (111) and (220) diffraction peaks are found from the XRD pattern, which may be caused by insufficient strength. The (200) diffraction peak exhibits significant asymmetry due to the appearance of a shoulder peak at 2θ = 43.8°, which is attributed to the formation of polymorphic structures (nanotwins and stacking faults)[77]. (Source data are provided as a Source Data file).

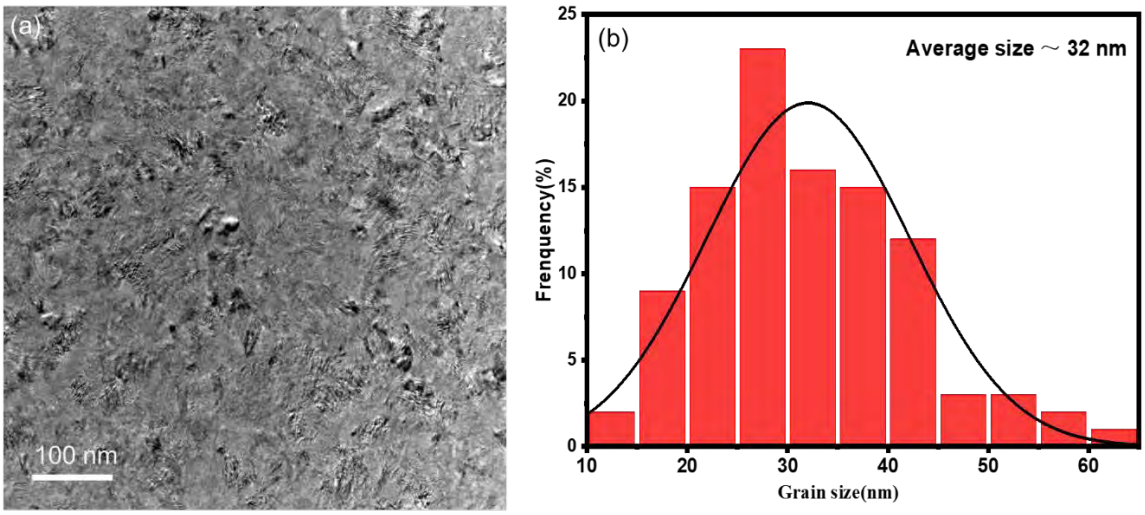

Supplementary Figure 3 Grain size distribution of CrN in TEM. (a) Grain morphology of the twin crystals showing an irregular grain morphology and no obvious grain boundaries and (b) Grain size distribution obtained by ImageJ showing that the average grain size is 32 nm (Source data are provided as a Source Data file).

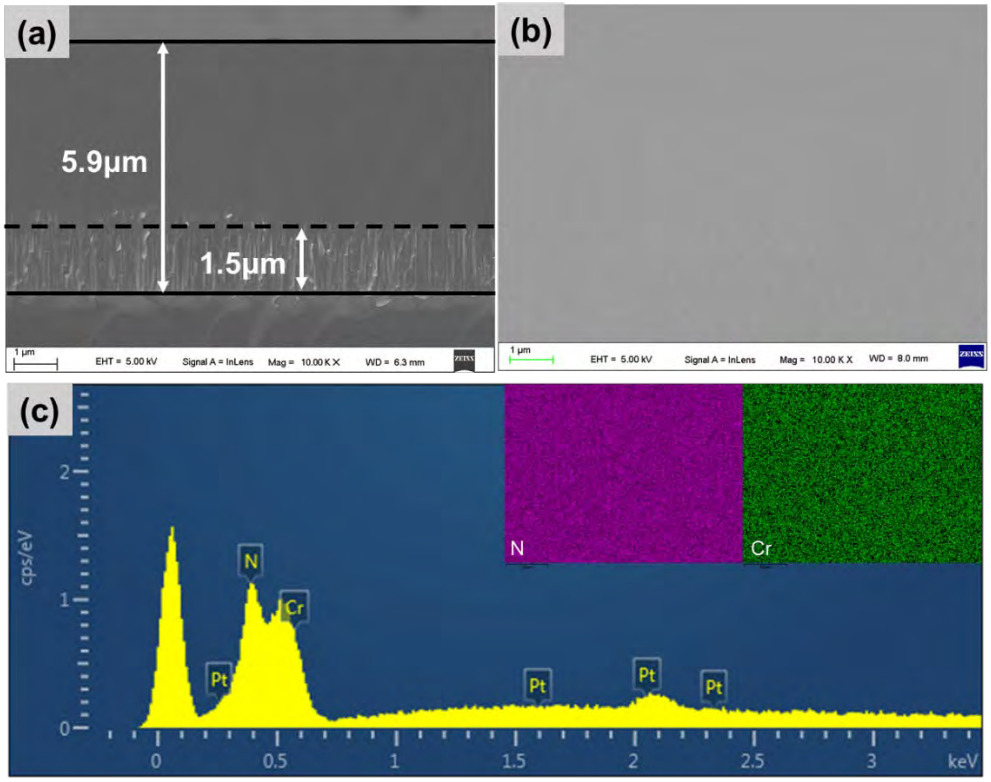

Supplementary Figure 4 Morphology and composition of CrN. (a) SEM image of the CrN cross-section; The coating is dense and can be divided into two parts: transition layer and CrN coating layer. The transition layer has a columnar structure, but the morphology of the CrN coating cannot be seen. The thickness of the CrN coating is about 4.4 μm, and the calculated deposition rate is 220 nm/min, which is larger than that produced by conventional HiPIMS. (b) CrN coating surface morphology. (c) EDS spectrum of the coating surface and elemental maps of N and Cr. The atomic ratio of Cr and N determined by EDS is about 50.2:49.8, which is close to 1:1.

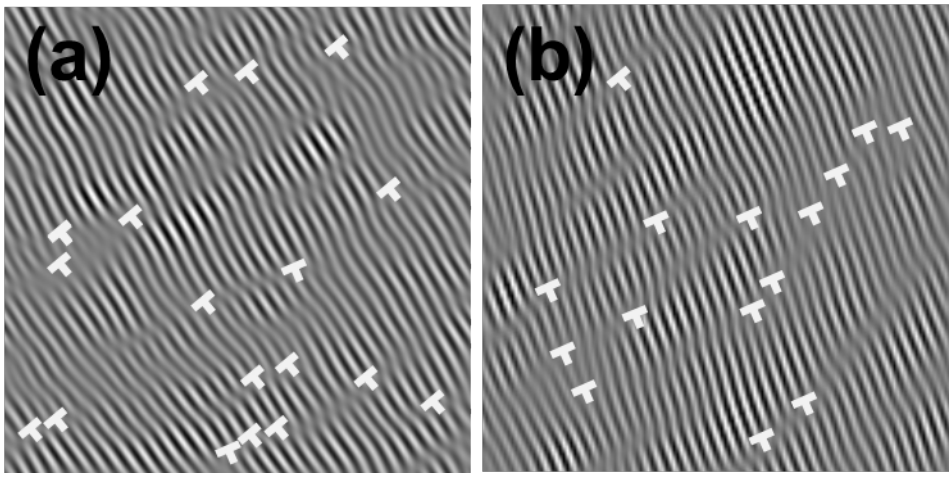

Supplementary Figure 5 IFFT of the selected zones. (a) Moiré fringes corresponding to Fig. 1(e) and (b) Moiré fringes corresponding to Fig. 1(f). The presence of dislocations can be clearly observed from the images.

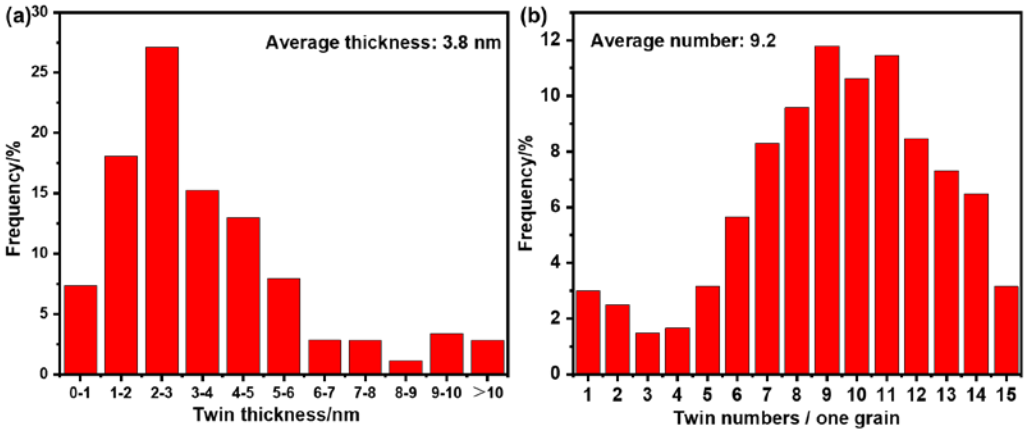

Supplementary Figure 6 Thickness and density distribution of nanotwins. (a) Thickness distribution of nanotwins. The average thickness of the twins is about 3.8 nm. (b) Distribution of TB in each grain. There are 9.2 TB in each grain on the average and the corresponding TB density is 9.0×10^{15} m^{-2}. (Source data are provided as a Source Data file)

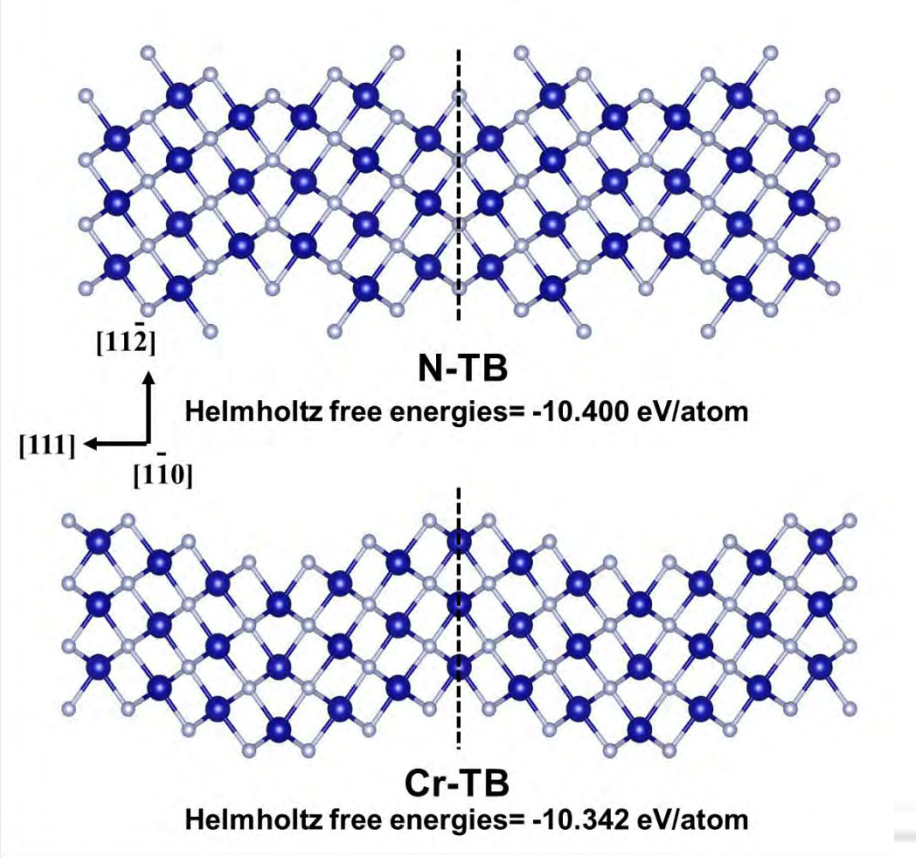

Supplementary Figure 7 Helmholtz free energies of the TBs. Helmholtz free energies of the TB with different atoms as the interface, where TB is the {111} surface. The blue and white dots represent Cr atoms and N atoms, respectively. According to first-principles derivation, the Helmholtz free energy of N-TB is -10.400 eV/atom and that of Cr-TB is -10.342 eV/atom.

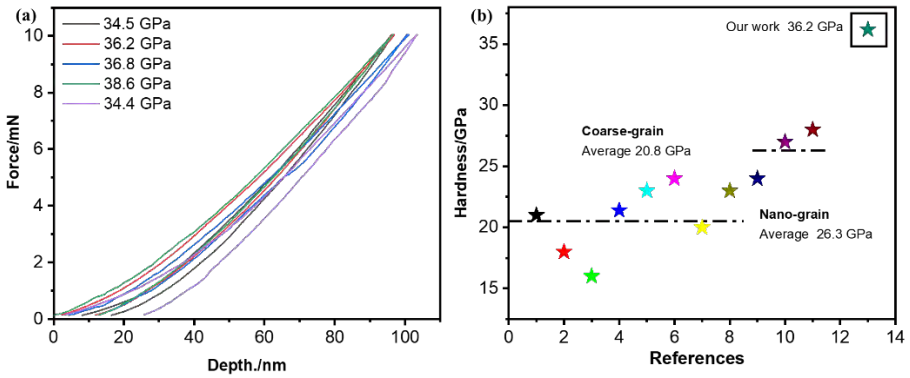

Supplementary Figure 8 Hardness of CrN coatings. (a) Loading and unloading curve; The average hardness of CrN is 36.2 GPa. (b) Hardness comparison. The average hardness of coarse CrN is 20.8 GPa, and the average hardness of nanocrystalline CrN is 26.3 GPa. The hardness of CrN in this work is about 75% higher than that of conventional CrN[78-86]. (Source data are provided as a Source Data file)

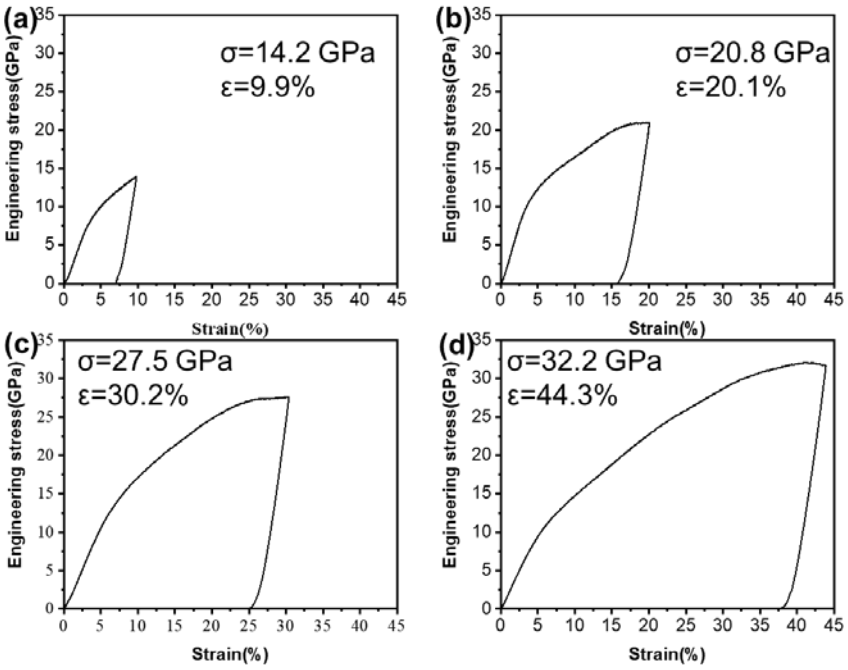

Supplementary Figure 9 Stress-strain curves for different deformation. (a) When the compression strain is 10%, the compressive strength is 14.2 GPa; (b) When the strain is 20%, the compressive strength is 20.8 GPa; (c) When the strain is 30.2%, the compressive strength is 27.5 GPa; (d) When the strain is 44.3%, the compressive strength is 32.2 GPa. (Source data are provided as a Source Data file)

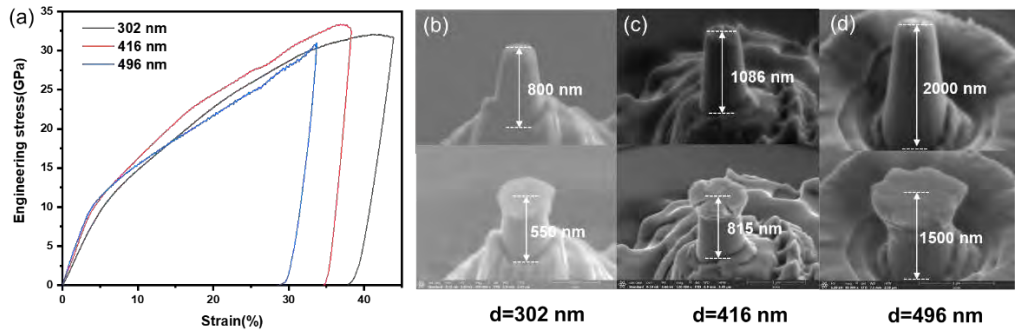

Supplementary Figure 10 Plasticity of micro-pillars with different diameters under compression. (a) Stress-strain curves of micro-pillars of different diameters, with the ultimate strain above 30% and ultimate stress up to 33 GPa. (b)-(d) SEM images before and after compression of micro-pillars with different diameters. Cracks can be observed from the top of the micro-pillars with d of 416 nm after compression. (Source data are provided as a Source Data file)

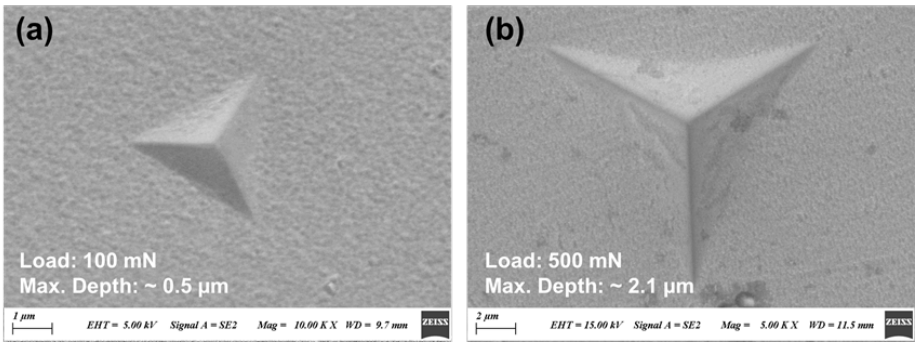

Supplementary Figure 11 Indentation morphology under different loads. (a) The indentation morphology at 100 mN by micro-indentation; (b) The indentation morphology at 500 mN by micro-indentation;

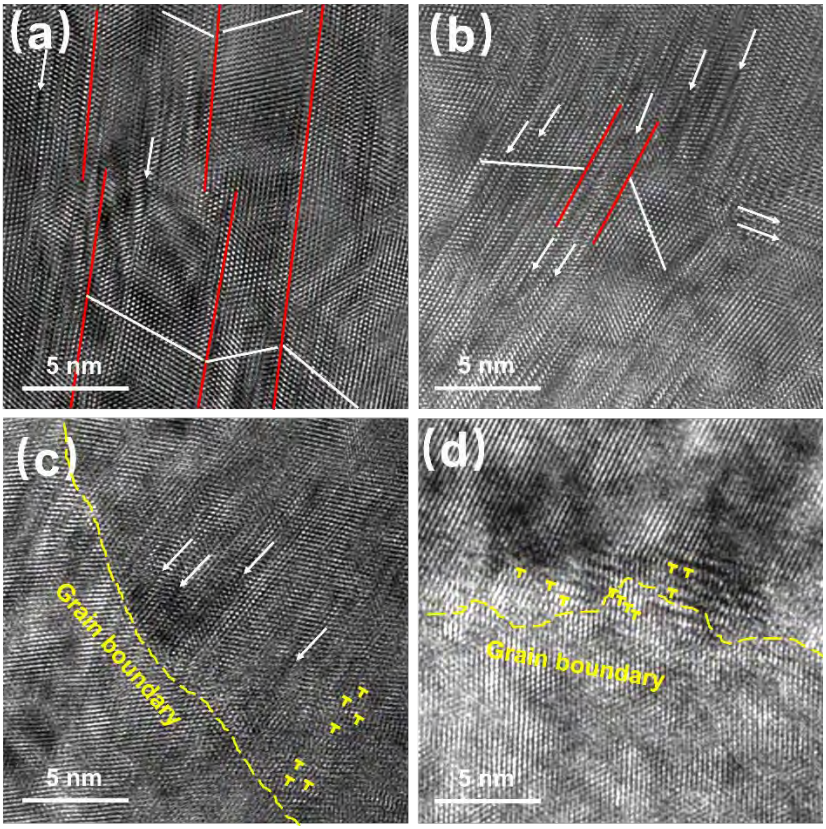

Supplementary Figure 12 Typical microstructures at the top region of the micropillar under different stages of compression. (a) Representative microstructure of the film at point A on the stress–strain curve; (b) Representative microstructure of the film at point B on the stress–strain curve; (c) Representative microstructure of the film at point C on the stress–strain curve; (d) Representative microstructure of the film when a crack appears at the top of the micropillar (Point D)

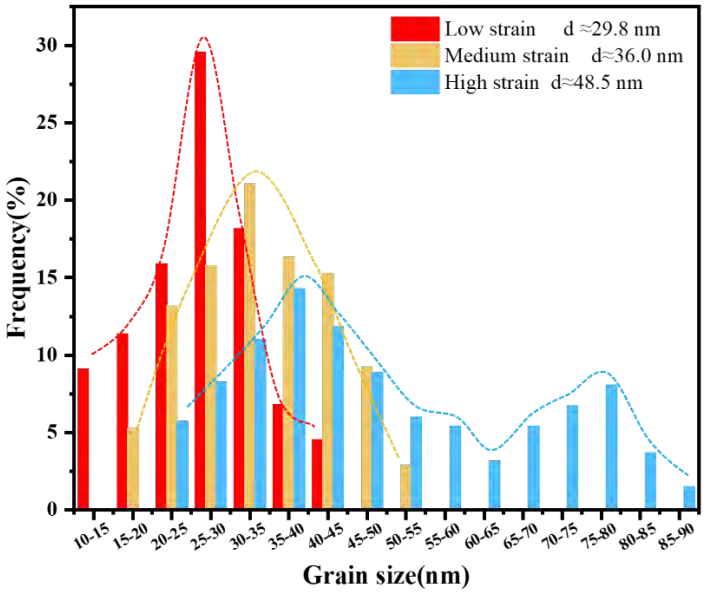

Supplementary Figure 13 Statistical histogram of the grain size in different deformation areas. The grain size in the low deformation region is about 29.8 nm, which is slightly smaller than the grain size (S3) calculated without deformation. This may be related to the region selected by micro statistics. The grain size in the medium deformation region is 36.0 nm and that in the high deformation region is 48.5nm. The grain size increases gradually with deformation. (Source data are provided as a Source Data file)

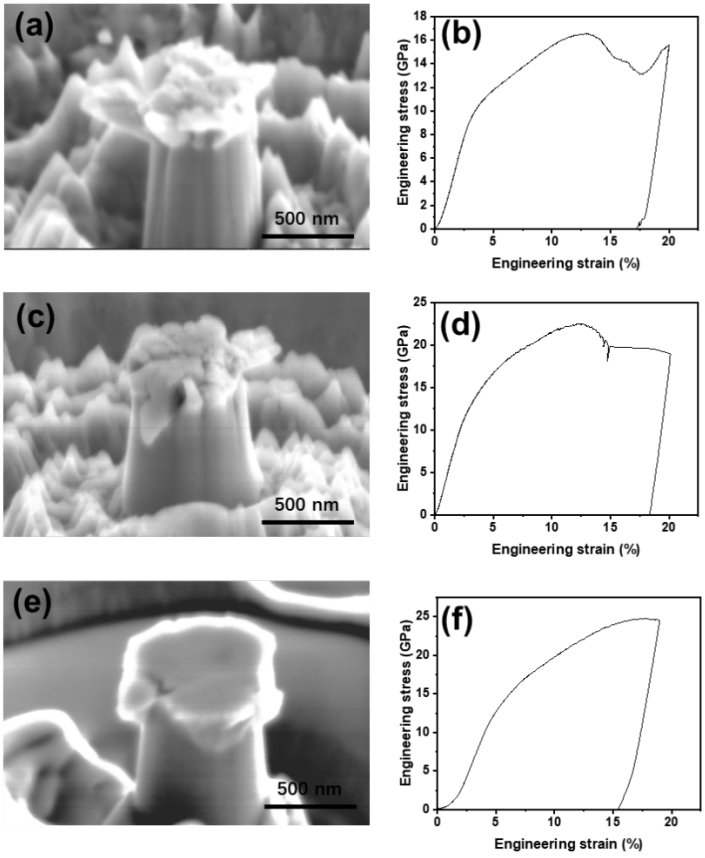

Supplementary Figure 14 SEM morphology and strain-stress curves of CrN samples with different twin densities after micro pillar compression (20%). (a) When the twin density is 1.8×10^{11} m^{-2}, the top of the micro pillar shows fragmentation traces. From the corresponding stress-strain curve (b), the engineering stress is about 16.5 GPa, and there has been fragmentation. (c) The twin density is 7.2×10^{13} m^{-2}. The top of the micro pillar shows the trace of fragmentation. From the corresponding stress-strain curve (d), the engineering stress is about 22.4 GPa. (e) Twin density is 3.1×10^{15} m^{-2}. The top of the micro pillar is upsetting, and the edge has a slight sign of fragmentation. From the corresponding stress-strain curve (f), the engineering stress is about 24.8 GPa. (Source data are provided as a Source Data file)

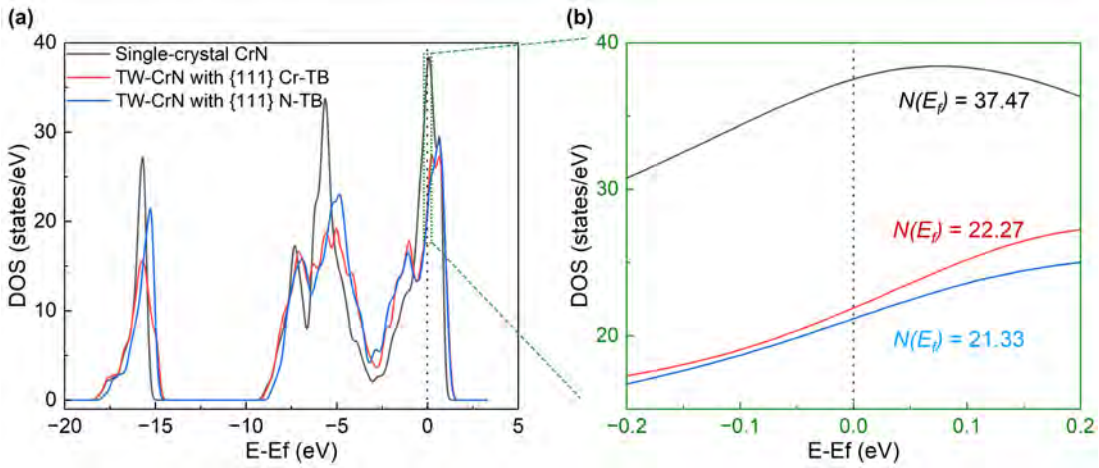

Supplementary Figure 15 Total DOS curves of different CrN. (a) Total DOS curves of single-crystal and twinned CrN. (b) Enlarged view of -0.2 eV to 0.2 eV, showing Fermi-level states. (Source data are provided as a Source Data file)

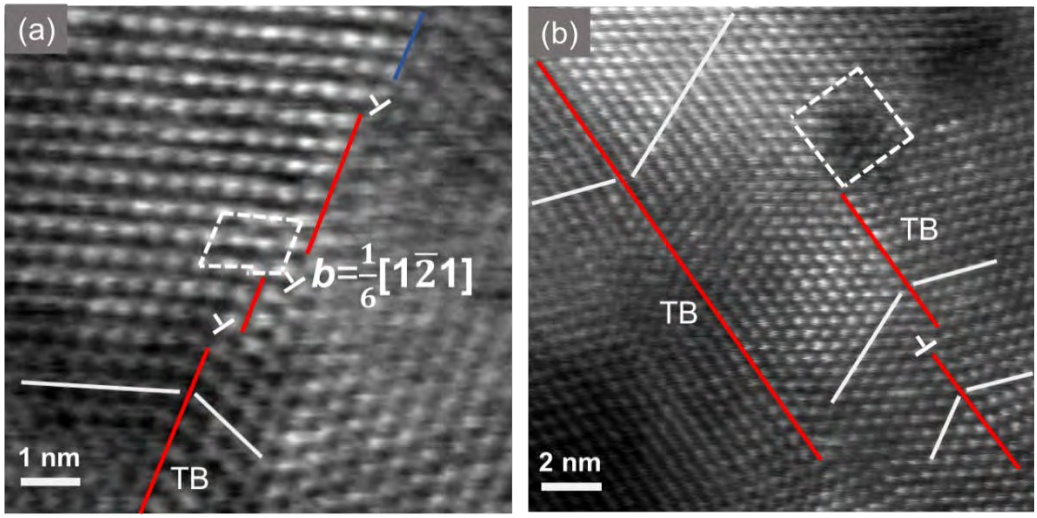

Supplementary Figure 16 Detailed diagram of the de-twinning process. (a) Partial dislocation in the TB disconnected region of the 1/6<1$\bar{2}$1> type and partial dislocation of this type at each TB disconnection. (b) When TB subsides, there are many partial dislocations at the end of TB. This indicates that detwinning is accompanied by 1/6<1$\bar{2}$1> and the formation of dislocation is similar to that of FCC metals during detwinning[87].

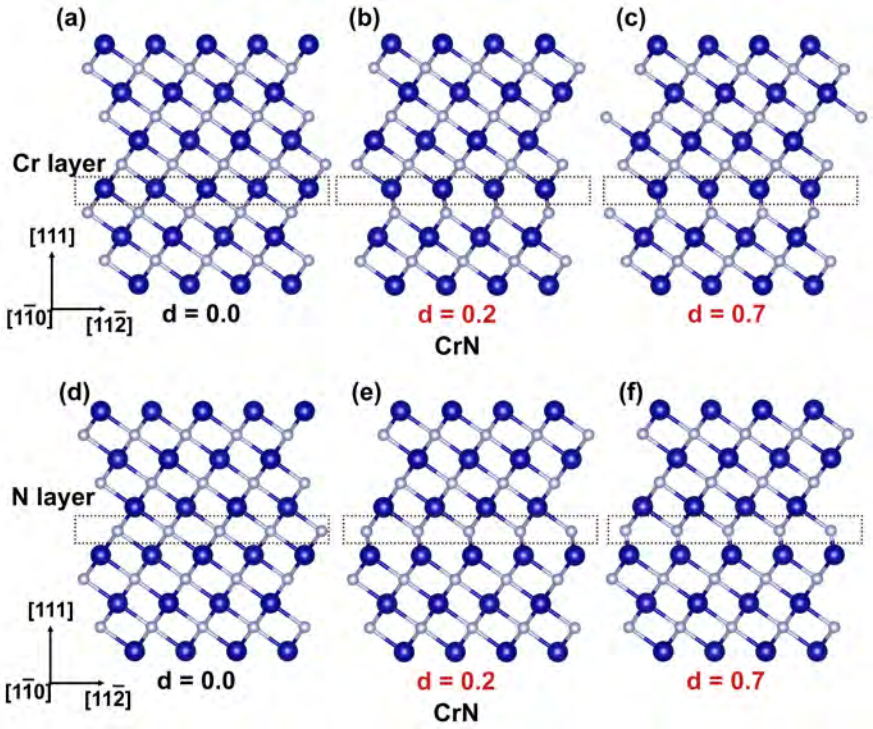

Supplementary Figure 17 Initial and deformed structures of single-crystal CrN at different sliding distance. (a) Initial structure for Cr as sliding interface; (b-c) Structure at a sliding distance of d = 0.2 and 0.7 for Cr as sliding interface. Unstable hexagonal rings appear during sliding; (d) Initial structure for N as sliding interface; (e) Structure at a sliding distance of d = 0.2 for N as sliding interface. Unstable hexagonal rings appear during sliding. (f) Structure at a sliding distance of d = 0.7 for N as sliding interface. Unstable hexagonal rings appear during sliding.

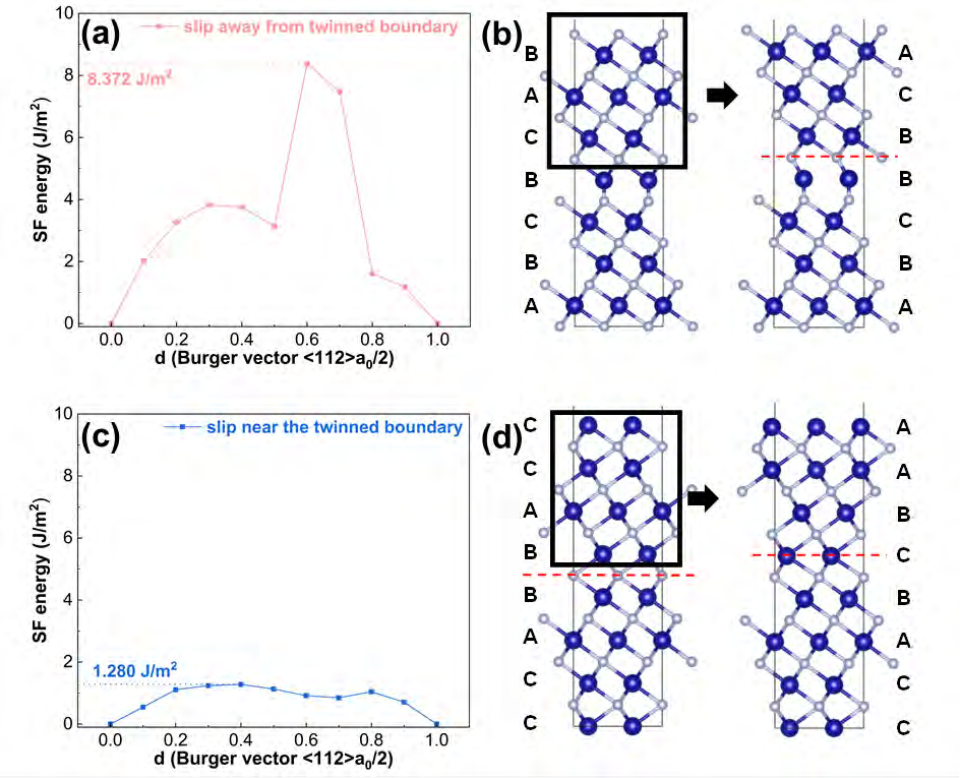

Supplementary Figure 18 Calculated results of generalized stacking fault energy. (a) slip away from the twinned boundary and its schematic diagrams of the slip (b). (c) slip near the twinned boundary and its schematic diagrams of the slip(d). (Source data are provided as a Source Data file)

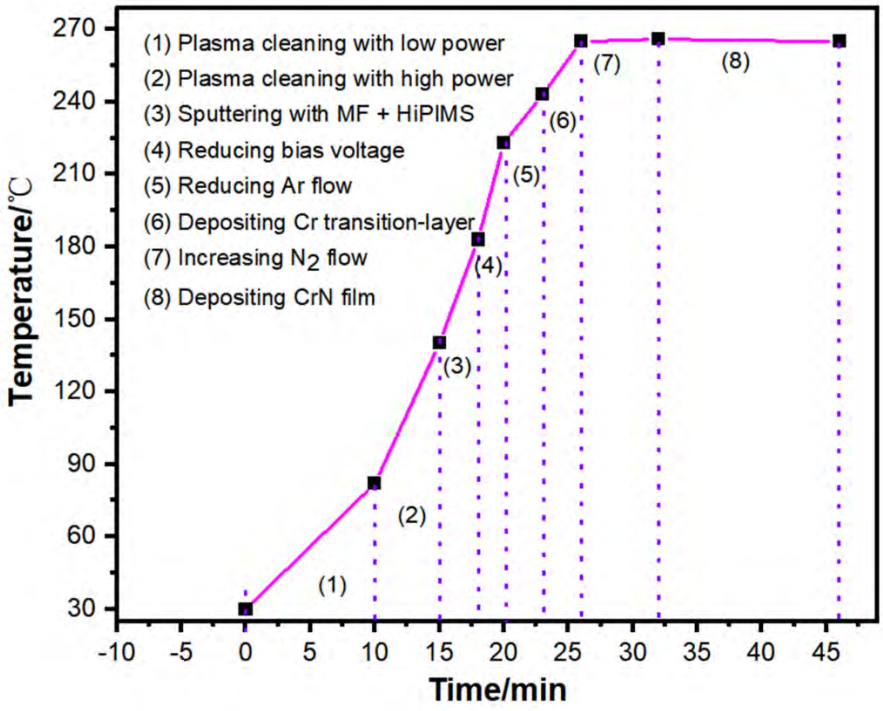

Supplementary Figure 19 Deposition process and temperature change of the CrN coating. Deposition can be divided into the cleaning stage (including low-power cleaning (1) and high-power cleaning (2)) and the bias in this stage is -650 V. The second stage is transition layer deposition (3)-(7), during which the bias decreases from -650 V to -100 V and the nitrogen flow increases to 11 sccm at a rate of 30 s/sccm. The final stage is CrN deposition. The HiPIMS power is 3.5 kW (frequency 50 Hz, pulse width 300 μs) and the deposition time is 20 min. During deposition, the temperature of the substrate increases gradually and is finally maintained at 270°C. (Source data are provided as a Source Data file)

Supplementary Table 1 The electrical resistivity of common metals and ceramics

	Materials	Electrical Resistance (Ω·cm)	Reference
Metals	Al	3.57×10^{-6}	88
	Ag	1.59×10^{-6}	89
	Fe	1.0×10^{-5}	89
	Cu	1.66×10^{-6}	89
	Au	2.0×10^{-6}	90
TMO	Al_2O_3	2.0×10^{13}	91
	ZnO	1.18×10^{2}	92
	ZrO_2	5×10^{13}	93
	TiO_2	7×10^{6}	94
TMC	CrC	4.8×10^{-4}	95
	CrC	3.2×10^{-4}	96
	TiC	0.85×10^{-4}	97
	TiC	0.80×10^{-4}	98
TMN	AlN	4.5×10^{15}	99
	AlN	8.1×10^{17}	100
	CrN	1.49×10^{-2}	101
	CrN	7.5×10^{-4}	102
	TiN	4.5×10^{-5}	103
	TiN	3.3×10^{-5}	104
	TiN	1.5×10^{-5}	105
---	BN	1.1×10^{9}	106
---	Si_3N_4	1×10^{14}	107
---	Si_3N_4	1×10^{15}	108
---	Diamond	5×10^{10}	109
TMN	NT-CrN	3.3×10^{-4}	This work

Supplementary Table 2 The engineering strain and strength of different materials

	Materials	Engineering Strain (%)	Engineering Strength (GPa)	Reference
Metals	Al	24	0.23	40
Metals	Nb	27	0.7	41
Metals	Fe	11	1.8	42
Metals	Cu	29	0.6	43
TMO	ZrO_2	5.8	8	43
TMO	ZnO	5	3.3	44
TMO	Al_2O_3	1.0	4.0	45
TMO	CeO_2	1.3	1.72	46
TMO	ZrO_2	61	23.0	38
TMC	Ti_2AlC	0.96	0.91	47
TMC	Ti_2AlC	1.13	1.02	48
TMC	Cr_2AlC	0.61	1.16	49
TMC	TaC	45.0	16.0	36, 37
TMN	TaCN	37.0	17.0	39
TMN	AlN	1.4	4.35	50
TMN	GaN	11	12.5	51
TMN	AlCrSiN	11.2	5.5	52
TMN	CrN	6.1	5.7	53
---	BN	2.2	0.11	53
---	BN	1.9	0.08	53
---	BN	14	0.63	54
---	Diamond	1.37	16	45
---	Diamond	1.92	20	45
---	Diamond	1.19	10	55
---	Diamond	7.0	120	56
---	Diamond	13	66	56
TMN	NT-CrN	44.3	32	This work

Supplementary Table 3. The elastic constant C_{11} and C_{33}, bulk modulus (B), shear modulus (G), and elastic modulus (E) for twinned CrN with and without N vacancy, as well as single-crystal CrN. The units of all these values are GPa.

	C_{11}	C_{33}	C_{44}	B	G	E
TW-$Cr_{24}N_{24}$ {111}Cr	508.80	593.06	156.78	334.60	159.44	412.77
TW-$Cr_{24}N_{23}$ {111}Cr	544.13	586.74	163.25	345.99	161.48	419.23
TW-$Cr_{24}N_{24}$ {111}N	526.89	610.22	221.56	340.11	185.83	471.60
TW-$Cr_{24}N_{23}$ {111}N	540.77	585.50	208.37	343.24	180.26	460.22
Single crystal $Cr_{24}N_{24}$	405.68	390.68	130.38	278.32	60.91	170.31

References

[77] Yue, Y., *et al.* Hierarchically structured diamond composite with exceptional toughness, Nature, 582, 370-374 (2020).

[78] Elangovan, T., *et al.* Nanostructured CrN thin films prepared by reactive pulsed DC magnetron sputtering, Mat. Sci. Eng. B, 167, 17-25(2010).

[79] Sánchez-López, J. C., *et al.* Tailoring CrN_x stoichiometry and functionality by means of reactive HiPIMS, Surf. Coat. Tech., 401, 126235(2020).

[80] Kong, Q., *et al.* Composition, microstructure, and properties of CrNx films deposited using medium frequency magnetron sputtering, Appl. Surf. Sci., 257, 2269-2274 (2011).

[81er pulsed magnetron discharge plasma immersion ion implantation and deposition, Appl. Surf. Sci., 258, 242-246 (2011).

[82] Warcholinski, B., *et al.* Structure and properties of CrN coatings formed using cathodic arc evaporation in stationary system, T. Nonferr. Metal. SOC., 29, 799-810 (2019).

[83] Lee, J., *et al.* The mechanical properties evaluation of the CrN coatings deposited by the pulsed DC reactive magnetron sputtering, Surf. Coat. Tech., 200, 3330-3335(2006).

[84] Lin, J., *et al.* A comparison of the oxidation behavior of CrN films deposited using continuous dc, pulsed dc and modulated pulsed power magnetron sputtering, Surf. Coat. Tech., 206, 3283-3290 (2012).

[85] Ferreira, F., *et al.* CrN thin films deposited by HiPIMS in DOMS mode, Surf. Coat. Tech., 291, 365-375 (2016).

[86] Gui, B., *et al.* Influence of N_2 flow rate on microstructure and properties of CrN_x ceramic films prepared by MPP technique at low temperature, Ceram. Int., 47, 20875-20884(2021).

[87] Wang, J., *et al.* Detwinning mechanisms for growth twins in face-centered cubic metals, Acta Mater., 58, 2262-2270 (2010).

[88] Kaya, H. Dependence of electrical resistivity on temperature and composition of Al–Cu alloys, Mater, Res. Innov., 16, 224-229(2012).

[89] Amin, N. A. A. M., *et al.* Effect of Ag content and the minor alloying element Fe on the electrical resistivity of Sn–Ag–Cu solder alloy, J. Alloys Compd., 599,114-120(2014).

[90] Aji, L. B. B., *et al.* Sputtered Au–Ta films with tunable electrical resistivity, J. Phys. D: Appl. Phys., 54, 075303(2020).

[91] Nakamichi, M., *et al.* Out-of-pile characterization of Al_2O_3 coating as electrical insulator, Fusion Eng.Des., 58, 719-723(2001).

[92] Zhang, Y. *et al.* Microstructure and temperature coefficient of resistivity for ZnO ceramics doped with Al_2O_3, Mate. Lett., 60, 2522-2525(2006).

[93] Santerre, F., *et al.* Properties of TiC thin films grown by pulsed laser deposition, Appl. Surf. Sci., 148, 24-33(1999).

[94] Kuo, D. H., *et al.* Characterization of nonstoichiometric TiO_2 and ZrO_2 thin films stabilized by Al_2O_3 and SiO_2 additions, J. Vac. Sci. Technol. A., 21, 1996-2002(2003).

[95] Groudeva-Zotova, S., *et al.* Phase composition of Cr–C thin films deposited by a double magnetron sputtering system, Surf. Interface Anal., 30, 544-548(2000).

[96] Andersson, M., *et al.* Deposition and characterization of magnetron sputtered amorphous Cr–C films, Vacuum, 86, 1408-1416(2012).

[97] Aihaiti, L., *et al.* Effect of annealing temperature on microstructure and resistivity of TiC thin

241 films, Coatings, 11, 457(2021).
242 [98] Santerre, F., *et al.* Properties of TiC thin films grown by pulsed laser deposition, Appl. Surf.
243 Sci., 148: 24-33(1999).
244 [99] Yoshikawa, J., *et al.* Effects of samarium oxide addition on the phase composition,
245 microstructure, and electrical resistivity of aluminum nitride ceramics, J. Am. Ceram. Soc., 88,
246 3501-3506(2005).
247 [100] Shin, Y. R., *et al.* Structural and electrical properties of ternary Ru–AlN thin films prepared
248 by plasma-enhanced atomic layer deposition, Mater. Res. Bull., 47, 790-793(2012).
249 [101] Wu, H., *et al.* Enhancing Electrical Conductivity and Corrosion Resistance of CrN Coating
250 by Pt Addition, Coatings, 11, 1479(2021).
251 [102] Gharavi, M. A., *et al.* Microstructure and thermoelectric properties of CrN and CrN/Cr_2N thin
252 films, J. Phys. D: Appl. Phys., 51, 355302(2018).
253 [103] Cheng, Y. H., *et al.* Electrical properties of TiN films deposited by filtered cathodic vacuum
254 arc. J. Vac. Sci. Technol. B., 20, 2000-2006(2002).
255 [104] Angadi, M. A., *et al.* The effect of the deposition rate on the electrical resistivity of thin tin
256 films, Thin Solid Films, 78, 299-302(1981).
257 [105] Kim, K. J., *et al.* Highly conductive SiC ceramics containing Ti_2CN, J. Eur. Ceram. Soc., 34,
258 1149-1154 (2014).
259 [106] Gerhardt, R. A., *et al.* Electrical properties of boron nitride matrix composites: III,
260 observations near the percolation threshold in BN–B_4C composites, J. Am. Ceram. Soc., 84, 2335-
261 2342(2001).
262 [107] Zschippang, E., *et al.* Electrical resistivity of Si_3N_4-SiC-$MeSi_2$ (Me= Nb, Mo, W, Zr)
263 composites, J. Ceram. Sci. Technol., 04,197-206(2013).
264 [108] Dow, H. S., *et al.* Thermal and electrical properties of silicon nitride substrates, AIP Adv., 7,
265 095022(2017).
266 [109] Vance, E. R., *et al.* The effect of heavy neutron irradiation on the electrical resistivity of
267 diamond, J. Phys. D: Appl. Phys., 5, L40(1972).
268